In-situ observations of volcanic ash clouds from the FAAM aircraft during the eruption of Eyjafjallajökull in 2010

Ben Johnson[1], Kate Turnbull[1], Phil Brown[1], Rachel Burgess[2], James Dorsey[2], Anthony J. Baran[1], Helen Webster[1], Jim Haywood[1,5], Richard Cotton[1], Z. Ulanowski[3], Evelyn Hesse[3], Alan Woolley[4], and Philip Rosenberg[4]

[1]Met Office, Fitzroy Road, Exeter, UK
[2]University of Manchester, School of Earth Atmospheric and Environmental Sciences, Oxford Road, Manchester, M13 9PL, UK
[3]University of Hertfordshire, Hatfield, Herts AL10 9AB, UK
[4]Facility for Airborne Atmospheric Measurement, Cranfield University, MK43 0AL, UK
[5]University of Exeter, College of Engineering Mathematics and Physical Sciences, North Park Road, Exeter, EX4 4QF, UK

Abstract

During April-May 2010 the UK Facility for Airborne Atmospheric Measurements (FAAM) BAe-146 aircraft flew 12 flights targeting volcanic ash clouds around the UK. Ash clouds were observed on every flight at altitudes between 2 – 8km. Due to safety considerations the aircraft only penetrated ash clouds forecast to have concentrations less than $2000\mu g/m^3$. Cloud and Aerosol Spectrometer (CAS) data showed peak ash concentrations in the range 200-2000 $\mu g/m^3$ on most flights during the May period. A peak value of 2000-$5000\mu g/m^3$ was observed over Scotland on 14 May, although with considerable uncertainty due to the possible contamination by ice. Aerosol size distributions within ash clouds showed a fine mode (0.1 – 0.6 μm) associated with sulphuric acid and/or sulphate, and a coarse mode (0.6 – 35μm) associated with ash. The ash mass was dominated by particles in the size range 1 – 10μm (volume-equivalent diameter), with a peak typically around 3 – 5μm. Electron-microscope images and scattering patterns from the SID-2H (Small Ice Detector) probe showed the highly irregular shape of the ash particles. Ash clouds were also accompanied by elevated levels of SO_2 (10 - 100ppbv), strong aerosol scattering (50 - 500 x 10^{-6} m^{-1}), and low Ångstrom exponents (-0.5 to 0.4) from the 3-wavelength nephelometer. Mass specific aerosol extinction coefficients (k_{ext}), based on the CAS size distribution varied from 0.45 – 1.06 m^2/g, depending on ash concentration and distance downwind. A representative value of 0.6 m^2/g is suggested for distal ash clouds (~1000km downwind) from the May period of this eruption.

1. Introduction

The eruption of the Icelandic volcano Eyjafjallajökull during April – May 2010 caused major disruption to European air travel due to prolonged emissions of volcanic ash and north-westerly flow bringing ash clouds over the UK and much of Europe. The main period of disruption occurred during 15 – 21 April (EUROCONTROL, http://www.eurocontrol.int) as a cloud of volcanic ash, originating from the initial and most powerful stage of explosive eruptions during 14 – 18 April, spread over much of Europe (Hogan et al., this issue; Ansmann et al., 2010; Gasteiger et al., 2011; Marenco and Hogan, this issue; Devenish et al., 2010; Dacre et al., this issue; Flentje et al., 2010; Lee et al., this issue). Further episodes of volcanic ash affected the UK and western parts of Europe from 2 – 22 May, after which explosive eruptions on Eyjafjallajökull subsided. The hazard that volcanic ash poses to

aviation is well-known (Prata and Tupper, 2009; Guffanti et al., 2010a) and has led to major air-travel space closures in the past (e.g. Casadevall 1994; Guffanti et al., 2010b), though none of these were on the scale experienced over Europe in 2010.

Throughout the eruption of Eyjafjallajökull the London Volcanic Ash Advisory Centre (VAAC) provided guidance to the National Air Traffic Services (NATS) and UK Civil Aviation Authority (CAA) based on ash forecasts produced by the Met Office Numerical Atmospheric-Dispersion Modelling Environment (NAME). NAME was configured to forecast ash concentrations within three different flight levels; surface – FL200, FL200-FL350 and FL350-FL550, where each unit FL (flight level) is equivalent to 100 feet assuming the International Civil Aviation Organization (ICAO) standard atmosphere. Initially the ash cloud was defined as regions with significant levels of ash based on the Volcanic Ash Forecast Transport and Dispersion (VAFTAD) table and nominal modelled release rates (Leadbetter and Hort, 2011; Witham et al., 2007). It was later deduced that the threshold used to identify the ash cloud extent corresponded to an estimated ash concentration of the order of $200\mu g/m^3$. Following agreements on engine tolerance thresholds (EU 2010) three concentration bands were established: $200\text{-}2000\mu g/m^3$ (low-risk), $2000 – 4000 \ \mu g/m^3$ (medium risk) and $> 4000 \ \mu g/m^3$ (high risk).

The European volcanic ash incident of April-May 2010 was also unprecedented in the number of research-quality measurements that were made of airborne volcanic ash across Europe and the north-east Atlantic (for an overview see Haywood et al., this issue and references therein). Prior to the 2010 eruption of Eyjafjallajökull intensive measurements of airborne volcanic ash have been rather limited. Previous airborne in-situ measurements of volcanic ash include the incidental sampling from the eruption of Hekla, Iceland, during 2000 (Hunton et al., 2005; Rose et al., 2006), sampling of plumes from US volcanoes Mt. Baker (Radke et al., 1976), Mt. St. Helens (Hobbs et al., 1982), and Mt. Redoubt (Hobbs et al., 1991), and sampling of plumes from the Guatemalan volcanoes Pacaya, Fuego and Santiaguito (Rose et al., 1980). Many other airborne observational studies have investigated the emission of volcanic gases and production of secondary aerosols, generally from quiescent or non-explosive eruptions (see Carn et al., 2011 for a recent review).

Observations of airborne ash from the eruption of Eyjafjallajökull during April – May 2010 were made from a number of atmospheric research aircraft (Schumann et al., 2011; Royer et al., 2011; Bukowiecki et al. 2011; EUFAR 2010) including the UK's BAe-146-301 Atmospheric Research Aircraft that is managed by the Facility for Airborne Atmospheric Measurements (FAAM). Observations also included combinations of ground-based lidars and sunphotometers (Marenco and Hogan this issue; Hogan et al., this issue; Ansmann et al., 2010; Gasteiger et al., 2011; Chazette et al., this issue), ground-based in-situ sampling (Flentje et al., 2010; Bukowiecki et al. 2011) and a balloon ascent (Harrison et al., 2010). In addition, satellite remote sensing products were used operationally and explored in post-event analysis (Clarisse et al., 2010; Francis et al., this issue; Newman et al., this issue; Millington et al., this issue; Baran et al., this issue). The remote sensing measurements made by the FAAM aircraft are detailed in Marenco et al., (this issue), and Newman et al., (this issue). A comparison of FAAM aircraft in-situ measurements with those made by the Deutsches Zentrum für Luft- und Raumfahrt (DLR) Falcon 20E atmospheric research aircraft is presented in Turnbull et al. (this issue). Whilst many of these observations were gathered with an immediate priority of verifying the presence, geographic extent and maximum mass concentration of ash clouds, the datasets serve as a major opportunity for research into the properties of airborne volcanic ash, the development of in-situ measurement and remote sensing capabilities (including satellite data products), and the validation of ash emission and dispersion models.

A large number of ash mass concentration estimates are compared with NAME dispersion model forecasts in Webster et al. (this issue). Also, Stohl et al. (2010) use a mixture of

airborne and satellite observations to constrain and evaluate simulations of volcanic ash emission and dispersion via the FLEXPART Lagrangian particle dispersion model. The results from each of these studies show broad agreement in the magnitude of modelled and observed ash mass concentrations despite large uncertainties in both the measurements and modelling of volcanic ash. Webster et al. also highlight the large discrepancies that can arise when comparing modelled and observed ash concentration due to even smaller errors in the timing and/or position errors of ash clouds. Such errors are in some cases a clear reflection of errors in numerical weather prediction model fields (Devenish et al., 2010; Stohl et al., 2011; Dacre et al., this issue; Grant et al., this issue; Devenish et al., this issue). On the other hand, the specification of emission source strength, near-source fallout, the relationship between model predicted mean concentrations over large volumes and localised peak concentrations unresolved by the model, and the vertical profile of ash emission also appear to be dominant sources of model uncertainty and model-measurement discrepancy in the above studies. Both Grant et al. (in prep.) and Devenish et al. (this issue) also show that reducing particle sizes (bringing the prescribed size distribution closer in line with the FAAM aircraft measurements that are reported here) improves the forecast position of ash clouds on certain occasions, due to the reduction of sedimentation rates. Other important but less dominant sources of model uncertainty include the treatment of vertical and horizontal turbulent mixing (Devenish et al., this issue).

This study presents in-situ measurements recorded aboard the FAAM aircraft during a series of flights investigating ash clouds around the UK from 20 April to 18 May. The paper provides an overview of the FAAM aircraft flights (section 2), aircraft instrumentation (section 3), the methods used to derive ash mass concentration (section 4), and the physical and optical properties of ash (section 5).

2. FAAM aircraft flights

2.1 Overview of the FAAM aircraft deployment

The FAAM aircraft was deployed during April-May 2010 to investigate volcanic ash clouds in the region around the UK that were affecting domestic and international air travel. This unplanned deployment brought the aircraft out of scheduled maintenance and into service on 20 April. A total of 12 flights were conducted on 9 separate days between 20 April – 18 May (see Table 1), making a total of approximately 54 flight hours. These included 9 full length flights of 5 -5.5 hours and three shorter flights of 1-2 hours. The primary objectives of all flights were to investigate the mass concentrations of ash and the geographic and vertical extent of those ash layers. The three shorter flights (B522, B525, B528b) were conducted to increase time in regions of interest and / or reposition the aircraft to an alternate airfield. The main airfields used were Cranfield (Central England: 52.1°N, 0.6°W), Prestwick (South-west Scotland: 55.5°N 4.6°W), Cambridge (Central-Eastern England: 52.2°N 0.2°E) and Nantes (Northern France: 47.2°N 1.6°W) (see Table 1).

As a four turbine-engine driven aircraft, the FAAM aircraft was subject to the same stringent safety criteria as applied to aircraft operating under CAA regulations. On the flights during 20 – 21 April (B521-B523) the FAAM aircraft therefore avoided penetrating ash clouds and focussed on remote sensing of ash layers from high altitudes (> FL200 ~ 6km) using the lidar. This ash avoidance policy was to satisfy CAA and internally agreed limits that were in place at that time. From 22 April onwards volcanic ash exposure safety limits were specified, and FAAM research flights were permitted to profile through ash layers provided NAME forecast ash concentrations were below 2000 $\mu g/m^3$. Avoidance measures were taken if real-time in-situ monitoring showed concentrations approaching this threshold. This led to the aircraft targeting zones where forecast volcanic ash concentrations were in the range 200-2000 $\mu g/m^3$.

2.2 Flight objectives
The main objectives of the ash flights were:
- To provide near real-time guidance on the spatial extent and mass concentration of ash clouds over the UK region (for the CAA and the National Air Traffic Service (NATS), Met Office and London VAAC).
- To validate NAME simulations of ash dispersion (during and post-event analysis).
- To investigate the physical, chemical and optical properties of transported volcanic ash for improvements in modelling, measurement and remote sensing capabilities.
- To explore relationships between ash mass, aerosol scattering and SO_2 concentration.

3. Instrumentation & modelling

The FAAM aircraft was equipped with a comprehensive range of instruments measuring standard meteorological parameters, aerosol and cloud properties, concentrations of key gaseous chemical species, solar and terrestrial radiation. A 355nm lidar was also used to remotely sense aerosol and cloud below the aircraft. A summary of these instruments is provided in table 2. This study focuses on the in-situ characterization of the ash and the instruments relied on for this study are described below. A general description of meteorological and other basic aircraft instruments can be found at www.faam.ac.uk and in Renfrew et al. (2009).

3.1 PCASP (fine-mode aerosol)
Concentrations of fine aerosols within the size range 0.1 – 3.0 μm (nominal diameter) were measured using a wing-mounted Particle Measuring System (PMS) Passive Cavity Aerosol Spectrometer Probe 100X (PCASP), with SPP200 electronics. The PCASP sizes particles based on the scattering of a 630 nm laser beam across scattering angles of $35 – 145^{o}$. The PCASP instrument was calibrated during the flight period using laboratory generated ammonium sulphate, size-segregated by a differential mobility analyser. The calibrated bin boundaries were corrected assuming a refractive index of 1.43 + 0i, based on the properties of sulphuric acid. We assume this to be the dominant fine-mode aerosol species within volcanic ash clouds where, in our observations SO_2 concentrations often remained highly elevated (e.g. > 10 ppbv). Sulphate, nitrate, and other components were also likely to have contributed to the fine mode as found by Schumann et al. (2011), in addition to variable amounts of water. However, due to heaters within the PCASP the measured aerosol was unlikely to have contained appreciable water. The refractive index of such a mixture is likely not far from the value we assume. The fine-mode aerosols are assumed to be spheres enabling the use of Mie theory to calculate scattering properties.

3.2 CAS (coarse-mode aerosol)
Concentrations of coarse aerosols of nominal diameters 0.6 – 50μm were measured using the Cloud and Aerosol Spectrometer (CAS), a component of the Droplet Measurement Technologies (DMT) Cloud Aerosol and Precipitation Spectrometer (CAPS) probe (Baumgardener et al., 2001). The CAS is a wing-mounted open-path optical particle counter. The CAS uses forward scattering $(4 – 12^{o})$ of a 680 nm laser beam to size particles. The CAS was calibrated by the manufacturer using a combination of PSL spheres (for d < 2μm), borosilicate glass beads (2μm $\leq$ d < 20μm) and soda lime glass beads (20μm < d < 50μm). The larger size bins (d $\geq$ 10μm) were checked pre-flight using glass beads and found to be sizing well with discrepancies no greater than the typical diameter spacing between adjacent bins (~15%). Mie theory is then used to calculate the scattering cross-section of the calibration spheres across the instrument's 4 -12° forward scattering angular detection range. This provides a calibration relating the amplitude of the instrument's response to particle scattering cross-sections. Using Mie theory the nominal size bin limits can then be defined in terms of the diameter of water droplets having the same scattering cross-section. However, in

this study the bin boundaries are defined in terms of the volume-equivalent diameter of irregularly-shape ash particles via a more complex treatment of scattering (as outlined in section 4.2).

The CAS data was also quality checked by examining the distribution of signal amplitudes in each gain stage from the raw particle-by-particle data. The use of three gain stages is required to span the very large range of scattering amplitudes (~4 orders of magnitude) that arise across the CAS size range. In this way the measurement of aerosol size is partitioned into three size ranges. The analysis revealed dips in the histogram of scattering amplitudes corresponding to the beginning of each of the three gain stages. These corresponded to slight dips in the derived aerosol size distribution in transitions between gain stages. This problem was attributed to the insufficient restoration of baseline voltages on each gain stage. A problem of this nature leads to some particles being oversized (placed in a bin too high for their true size), but would not have led to over-counting or under-counting. Although no formal correction for this problem has been proposed a reasonable attempt has been made to adjust the data for this error. Within the post-flight data interpretation the signal amplitude thresholds for each bin were adjusted by assuming an increased voltage offsets on each gain stage. The voltage offsets were tuned to ensure a smooth and continuous distribution of signal amplitudes across the entire range of measured signal amplitudes. This correction did not alter the total number of particles, nor the number counted in each bin but led to changes in the lower and upper diameters for each size bin. Corrections for particle shape and refractive index are explained in section 4.2 and the sensitivity to those assumptions is assessed in section 5.5.1.

3.3 SID-2H (coarse-mode aerosol scattering patterns)
An improved version of the Small Ice Detector 2 (SID-2) (Hirst et al., 2001; Cotton et al., 2009) was also fitted and used to determine the scattering patterns and asphericity of particles of diameters > 2μm. SID-2 is an optical particle counter that measures the intensity of forward scattered light across scattering angles of $9 - 20^{\circ}$ and its azimuthal variation using independently sensed detector elements. The improved version, named SID-2H, uses for this purpose 28 elements of a multi-channel photomultiplier coupled via fiber-optics guides (Ulanowski and Schnaiter, 2011). Whilst the data from SID-2H can be used to estimate particle size distributions, the asphericity of the particle's scattering also gives clues to the particle shape and hence composition. Originally the SID instruments were developed to allow the discrimination between super-cooled water drops and ice crystals in the diameter range 1–24 μm. However, recent measurements in Saharan dust (Johnson and Osborne, 2011) have shown that SID-2H is capable of measuring the scattering from coarse mineral-dust particles (d > 2μm). The SID-2H instrument was calibrated using PSL (latex) spheres, as described in Cotton et al. (2009). This calibration is given in nominal diameters relevant to water spheres. However, due to various issues regarding signal amplification (gain), and triggering thresholds the sizing performance of the probe in these flights was uncertain. The SID-2H data is therefore used in this study mainly for qualitative examination of aerosol scattering patterns.

3.4 Nephelometer (aerosol scattering coefficients)
Aerosol scattering was determined at 3 wavelengths (0.45, 0.55, 0.70 μm) with a TSI 3563 nephelometer. Angular truncation errors were corrected following the super-micron relations in Anderson and Ogren (1998). The air sample is drawn from a Rosemount inlet with and transmitted through short pipes (< 2m) comprised of latex rubber infused with black-carbon. All components of the inlet and pipe-work are electrically conductive and earthed to prevent the build up of static charge that would lead to aerosol losses. The Rosemount inlet is not designed for aerosol sampling and as yet its sampling efficiency is not fully understood. When the TSI instrument was situated on the C-130 aircraft during the SHADE measurement campaign in 2000 (Tanré *et al.*, 2003), a significant correction had to be made to account for the loss of super-micron aerosol particles in the inlet/pipe-work (Haywood *et al.*, 2003).

Recent tests at FAAM (personal communication Jamie Trembath) suggests that the Rosemount inlet losses some particles greater than 5μm diameter but may oversample particles in the diameter range 1 – 5μm. Comparison of aerosol optical depths derived from the nephelometer when the TSI instrument was situated on the BAe-146 aircraft against Aerosol Robotic Network (AERONET) sun-photometers during DABEX (Osborne *et al.*, 2008) suggests either that the majority of super-micron dust particles are sampled or that the under and over sampling biases across the super-micron range compensated in that set of measurements. As correction factors for such sampling issue are not yet developed at the time of this study, no correction for super-micron particle losses was made.

3.5 Cloud ice measurements

Bulk ice water content was measured using a Nevzorov hot-wire probe (Korolev et al., 1998a). This has a heated conical collector facing into the airstream. Ice crystals are collected within this cone and then melted and evaporated. The collector is maintained at a constant temperature and the additional electrical power required for this in cloud is equated to the latent heat of evaporation of the cloud ice. The instrument has a sensitivity of around 0.002 gm^{-3}. The absolute accuracy is dependent on the removal of altitude- and temperature-dependent baseline drifts which are of order 0.005 gm^{-3} km^{-1}. Recent tests by Korolev (personal communication) have suggested that the standard collector may underestimate the true ice water content, especially for larger ice particles, by a factor of ~3. This is due to the loss of water mass from the collector prior to its evaporation due to a combination of particle bouncing or the splashing out of meltwater by subsequent incoming particles. This is alleviated in recent versions of the probe which use deeper collector cones but these were not fitted at the time of the flights described here.

The Cloud Imaging Probe (CIP) is an updated version of the 2D Optical Array Probe (Korolev et al., 1998b) manufactured by DMT. A 64-element array of photodiodes is illuminated by a laser beam. Ice crystals passing through the beam shadow the array. By means of sampling the array at a suitably high rate, a digitized shadow image of the particle is recorded. In the version described here (which is another part of the DMT CAPS instrument, see section 3.2 above), the optical magnification is such as to give a pixel resolution in the array-parallel direction of 15 μm and the instrument is referred to as the CIP-15. Images are processed to determine their linear dimensions and, by means of the use of suitable size-to-mass conversion factors, their mass. In the data described here, the size-mass factors are those given by Brown and Francis (1995) and the total ice water content is obtained by integration over the full size spectrum.

3.6 Filter measurements

The filter sampling system on board the FAAM aircraft is described by Formenti et al (2008), and consists of a thin-walled metallic inlet nozzle with a curved leading edge. The design was based on criteria for aircraft engine intakes at low Mach numbers (Andreae et al., 1988). This design reduces distortion of the pressure field at the nozzle tip and the resulting problems associated with flow separation and turbulence. A curved metallic pipe feeds the air sample into the cabin and directly into a short diffuser (~20cm) ahead of teflon stacked-filter units. Two of these inlet and filter systems are mounted in parallel. The aerosol intake system was designed so that rain and large cloud water droplets would be removed from the sampled air stream by inertial separation. The passing efficiency of the inlets has not been formally quantified. However, Chou et al. [2008] has shown that the number size distributions of the aerosols collected on the filters (counted by electron microscopy) extended up to 10μm diameters and were comparable to those measured by wing-mounted optical counters. Because the sampling is sub-isokinetic, a relative enhancement of the coarse particle fraction might be expected. Each SFU consisted of two 47mm Nucleopore filters of 10 and 1 μm pore diameter. Filters were exposed for extended periods (usually half or whole of a flight) to gain the sufficient mass loading but exposure was interrupted during passes through cloud or boundary layer aerosol to avoid contamination.

Scanning Electron Microscope (SEM) imagery and elemental analysis of the aerosol collected on the filters was carried out at the University of Manchester using a Phillips FEI XL30 Environmental Scanning Electron Microscope (ESEM) equipped with a Super Ultra-thin Window and EDAX™ automatic particle analysis software (Hand et al, 2010). The SEM was operated with the back-scatter detector and beam energy of 15kV (occasionally 20kV). After the initial focussing the SEM was controlled using the EDAX™ Genesis software to automatically image the required number of fields of view, scan and collect spectra for each automatically identified individual particle. For each individual particle several morphological features are recorded and also some information on the chemical composition is achieved from the spectra yielded from the energy dispersive x-ray (EDX). The chemical composition analysis is ongoing and will not be discussed here. However, initial results showed the dominant elements in the majority of the particles analysed were Si, Al, and Mg, and had signature compositions of volcanic ash. Fe was also observed in approximately half of these Si and Al containing particles. The presence of Ti, K and Ca was also detected in some of the particles though not necessarily simultaneously. A full description of the chemical and morphological characteristics of the sampled particles will be given in a separate paper (Burgess et al in prep).

3.6 Gas phase measurements
Gas phase chemistry measurements of sulphur dioxide (SO_2) were made using a Thermo Electron 43C Trace Level analyzer which relies on pulsed fluorescence (Luke, 1997). This has a detection limit of 0.005 ppbv and a precision of 1% or 0.2 ppbv (whichever is greater). The instrument was calibrated prior to the series of flights using bottled gas. This provides 10 second averages but loss of time resolution and time lag due to the low sample flow rate (0.5 L/min). Data was corrected by allowing a 25 second time lag relative to the real-time data (i.e. fast response instruments such as the wing-mounted OPCs). The effective time resolution of the data appears to be around 20 s making the data more suitable for identifying broad features (dz ~ 300m, dx ~ 10 km) during profiles or runs, or averages over ash cloud penetrations of at least 1 min.

3.7 AERONET data
AERONET data (Holben et al., 1998) were obtained from http://aeronet.gsfc.nasa.gov. The sites of Helgoland (54.2°N, 7.9°E), Brussels (50.8°N, 4.3°E), and Cabauw (52.0°N, 4.9°E) were selected for the period from 1500UTC on 17 May to 1800UTC on 18 May. Almucantar scans were used in conjunction with version 2 inversion algorithms to retrieve aerosol size distribution. The version 2 algorithm includes a representation for particle asphericity via randomly orientated prolate and oblate spheroids (Dubovik *et al.*, 2006).

3.8 NAME model
The Numerical Atmospheric-dispersion Modelling Environment (NAME) is a Lagrangian particle model that was used to simulate the dispersion of ash from the 2010 eruption of Eyjafjallajökull. It was driven by meteorological data from the global version of the Met Office's Unified Model (MetUM) with a spatial resolution of about 25km in mid latitudes and a temporal resolution of 3 hours. A full description of NAME and its set-up for simulations of ash from the 2010 Eyjafjallajökull eruption are given in Webster et al. (this issue). The dispersion simulations presented in this study are from a post-event simulation. The set-up was identical to that used operationally towards the end of the eruption except that analysed, as opposed to forecast, meteorological data was used. The mass emission rate was calculated using the continuous fit to the VAFTAD thresholds. The simulations are therefore an attempt to producing the best possible post-event analysis in the absence of data assimilation or user intervention. The mass emission rate is estimated from the observed eruption height using an empirical relationship between these two quantities. 95% of the erupted mass is assumed to fall-out near to the source (i.e. only 5% is assumed to survive into the distal ash cloud). Loss of ash due to gravitational settling of heavy particles and wet and dry deposition processes is

represented within NAME. A particle size distribution is used for volcanic ash based on measurements from explosive eruptions of Mount Redoubt, St Augustine and Mount St Helens as presented by Hobbs et al. (1991). Average concentrations are calculated over 6-hour time periods and over deep atmospheric layers (0 – FL200 [approx 0 – 6km], FL200 – 350 [approx 6 – 10.7km], FL350 – 500 [approx 10.7 – 15km]). The peak concentration likely to occur in these deep layers and 6-hour time periods is assumed to be a factor of 20 higher than the large-scale modelled mean concentration.

4. Derivation of ash particle size distribution and mass concentration from the CAS instrument

4.1 Method of deriving ash mass concentration

The aerosol size distribution was segregated into a fine mode (0.1 – 0.6μm), measured by the PCASP and assumed to be sulphuric acid aerosol, and a coarse mode (0.6 – 35μm), measured by the CAS and assumed to ash. The cut-off at 0.6μm was based on size-resolved chemical composition results from Figure 6 of Schumann et al. (2011) and the observed minima in the PCASP and CAS mass distributions (see section 5.3.1). In this study, only bins 2 – 26 of the CAS are used, covering volume-equivalent diameters of 0.6 – 35μm (see Table 2). The first bin was rejected as the lower limit of its diameter range was poorly defined. The largest four bins of the CAS (bins 27 – 30) were rejected from the analysis as these returned zero or negligible concentrations in cloud-screened data from ash plumes. The ash mass concentration was therefore derived by integrating the following equation:

$$M_{ash} = \rho_{ash} \sum_{i=2}^{26} N_i \frac{4}{3} \pi \left(\frac{d_{v,i}}{2} \right)^3 \tag{1}$$

where M_{ash} is the ash mass concentration (μg/m^3), N_i is the number concentration (m^{-3}) in size bin i of the CAS instrument spanning bins 2 – 26, ρ_{ash} is the density of ash, and $d_{v,i}$ is the equivalent-volume spherical diameter derived for size bin i (in the case of irregular particles this is the diameter of a sphere with equivalent volume). To ensure good particle counting statistics N_i was averaged over 10 second intervals (corresponding to horizontal flight path of 1.2 – 1.6km). Data points with $M_{ash} < 20$μg/m^3 were rejected from the analysis as these are likely affected by poor counting statistics and background aerosol. We assume a mass density of 2300 kg/m^3 for the ash to be consistent with the properties specified in the NAME dispersion model (Webster et al., this issue). This may be regarded as a low estimate compared to published values for solid volcanic glasses and minerals (typically 2350 – 3000 kg/m^3, e.g. Shipley and Wojcicki 1982; Sparks et al., 1997; Mastin et al., 2009; Gudmundsson et al., 2010; Schumann et al., 2011) but accommodates the possibility of air pockets within aggregates and larger particles (e.g. James et al., 2002, 2003). Volume-equivalent diameters were derived by modelling the optical properties of ash and the scattering response detected by the CAS instrument. As this requires assumptions on particle shape and refractive index three cases have been considered.

4.2 Refractive index and particle shape assumptions

In the default case "ash irregular" the ash is represented by irregular-shaped particles and a refractive index of 1.52 + 0.0015i, based on the mineral dust dataset of Balkanski et al. (2007) with the medium level of hematite (1.5%). Although the mineralogy of volcanic ash differs from that of desert dust estimates for the refractive index are similar. Current estimates for volcanic glasses and minerals suggest real parts between 1.50 – 1.60 and imaginary parts generally between 0.001 – 0.004i for the wavelengths around 600 - 700nm (Patterson 1981; Patterson et al., 1983; Pollack et al. 1973; Horwell 2007; Schumann et al., 2011; Oskarsson 2010; Hogan et al., this issue). The Balkanski et al. refractive index dataset has also proved successful in modelling upwelling solar and spectrally resolved longwave radiation when

compared with observations taken above ash layers from both from the FAAM aircraft and the Infra-red Atmospheric Sounding Interferometer (IASI) satellite instrument (Newman et al., this issue).

The irregularity of ash particle shapes have been represented using a method previously applied to mineral dust, as described in Osborne et al. (2011). This treated the particles as a mixture of hexagonal prisms (for $0.6 < d_v < 1.5$ μm), and polyhedral crystals (for $1.5 < d_v < 35$μm). The polyhedral model is based on Macke et al. (1996) which was originally applied to study the scattering properties of cirrus but has successfully been applied to large mineral dust aerosols by Kokhanovsky (2003) and Osborne et al. (2011). The scattering properties in this study were calculated from the Ray Tracing with Diffraction on Facets (RTDF) method (Hesse 2008). This differs from classical geometric optics by considering diffraction at facets additionally to diffraction at the projected cross-section and therefore describing size-dependence better, especially for the smaller sizes characteristic of the ash particles. Due to this, the calculations are different from the ones in Kokhanovsky (2003) even if the crystal geometry is the same. Although detailed analysis has not yet been performed to assess the applicability of this model to the volcanic ash, the fractal-like irregular shapes it uses are arguably a more realistic representation for ash than the smooth, compact and symmetrical geometry of spheres or spheroids. These shapes are evident in electron microscope images of volcanic ash for Eyjafjallajökull (see section 5.4.1 and Navratil et al., this issue). Newman et al. (this issue) show that interpreting the CAS data with this irregular shape model led to a better comparison between CAS mass loadings and IASI retrievals, compared to the interpretation of CAS with spheres. Further research would be required to refine the assumptions used in the polyhedral model based on statistical analysis of SEM images and/or SID-2H data.

Two spherical ash treatments are also used (Table 2) as sensitivity test. The "moderately absorbing ash sphere" has the same refractive index as the default "irregular ash" case ($1.52 + 0.0015i$), and the "highly absorbing ash sphere" is a case with refractive index raised to $1.59 + 0.004i$, following Schumann et al. (2011). The optical properties for the spherical ash cases were derived from Mie theory.

4.3 Cloud screening of ash data
All flight data were manually screened for cloud using a combination of evidence from: (1) visual observations reported from the flight deck, (2) hygrometers indicating saturation with respect to liquid water or ice, (3) significant returns ($> 10^{-3}$ g /m^3) from the NEVZOROV total water content probe, (4) sudden orders of magnitude increases in CAS particle volume dominated by particles of nominal diameters $10 – 50$μm, (5) an extension of the particle size distribution into diameters > 50μm on the SID-2H and CAPS Cloud Imaging Probe (CIP-15), indicative of ice aggregates and/or precipitation, (6) dramatic increases in CAS particle volume that were not correlated with, or highly disproportionate to the nephelometer aerosol scattering or SO_2 concentration. In water cloud and thick patches of cirrus, cloud was easily identifiable from the above indicators.

5. Results

5.1 Spatial distribution of ash and comparison with NAME forecasts
Figure 1 shows the flight tracks of the FAAM aircraft for flights B526 - B531 ($4 – 18$ May) with M_{ash} (the CAS estimate of ash mass concentration from eqn. 1) shown along each flight track. The earlier flights of B521 - B525 (20 - 22 April) are not shown as very limited in-situ sampling was conducted on those flight and observed ash concentrations did not exceed 30 μg/m^3. The majority of substantial ash concentrations (> 200 μg/m^3) were observed during the flights of $4 – 18$ May (B526-B531) and for this reason the results below focus mainly on these flights. The spatial distribution of the data in Figure 1 is shown in relation to ash

concentrations predicted by the NAME dispersion model. Flight plans tended to be spatial extensive to survey regions where ash had been forecast in concentrations above 200µg/m³, and/or SEVIRI imagery had suggested ash clouds. As significant portions of many of the flights were conducted at high altitudes, typically FL250 – 300 (7.5 – 9km, see Figure 2), to enable remote sensing by nadir pointing instruments, fair comparisons between M_{ash} and the model can only be made in those regions where a full vertical profile spanning the ash layer(s) was made (see Figure 2). Therefore the comparison in Figure 1 must not be taken at face value but must be interpreted carefully following the detailed flight-by-flight comments below. These NAME dispersion simulations indicate the maximum concentration likely in any particular region over a 6 hour time window and in a given altitude range, in this case from the surface to FL200 (~6km). Due to the chaotic and turbulent nature of the atmospheric flow at the volcanic source and during subsequent advection the NAME does not attempt to make a deterministic prediction of ash concentration fields downwind. Rather the simulated fields indicate the possibility (or risk) of encountering ash concentrations between certain limits in a broad time window and altitude band. The goal of this section is therefore to see if the maximum observed ash concentrations would have been anticipated given the best possible simulation from NAME. The FAAM in-situ ash concentration estimates are compared to NAME simulations in a more statistical manner in Webster et al. (this issue). Further comparisons between NAME and the aircraft in-situ and remote sensing data are given by Devenish et al. (this issue) for the 14ᵗʰ May case. Comparisons of the NAME simulations with FAAM lidar retrievals of ash mass are also shown in Marenco et al. (this issue).

B526 (4 May): Flight B526 surveyed an ash cloud over Wales, the Irish Sea and the Bristol Channel. The flight plan included three overpasses of a ground-based observing site at Aberystwyth (52.5°N, 4.1°W) to enable comparison of aircraft with ground-based lidar measurements (Marenco et al., 2011). The bulk of the in-situ measurements gathered during this flight are from a pair of profiles over the Irish Sea and a brief descent into an ash layer at 5km over the northwest tip of Wales (see Figures 1 & 2). These show the dispersion simulation to have correctly predicted an ash layer in those regions with an appropriate range of mass concentrations (60 – 200 µg/m³).

B527 (5 May): Flight B527 investigated an ash cloud encroaching from the northwest. The lidar and in-situ sampling during profiles reveal that some of the ash cloud extended further east over the UK than predicted in the NAME simulation (Figure 1). The excursion into the North Sea found the edge of the ash cloud (perceptible by lidar) at ~0° longitude. On this day most of the ash was found in a thin layer between 3 and 4km with peak concentrations of 200 – 600 µg/m³. Tenuous layers with concentrations 20 – 200µg/m³ were also encountered in a few locations at 7 – 8km (see Figure 1 & 2). The peak concentrations obtained during the profiles over the Irish Sea show good agreement with the NAME simulation but the final profile into Cranfield exceeds the simulated peak. This discrepancy was associated with a more limited eastwards progression of the modelled ash cloud than observed (see Marenco et al., this issue).

B528 (14 May): Flight B528 took the aircraft to the far north-west approaches of Scotland to investigate an ash cloud encroaching on Scottish airspace. This flight provided the most substantial quantity of in-situ sampling data and the highest ash concentrations of the series of flights presented here. The CAS observed higher ash concentrations than NAME simulated, particularly over Central and Southern Scotland. Peak estimates of ash concentration were difficult to disentangle from the influence of ice (appendix B) but are estimated to have reached 2000 - 5000µg/m³. Devenish et al. (2011) provides a full investigation of the ash dispersion simulations for this case study and their sensitivity to various modelling assumptions. The ash observations made over Central England 52 – 53°N were obtained around 1900UTC and fall outside the validity time of the NAME simulation in Figure 1 (1200

-1800 UTC). This is a source of discrepancy between those observations and the NAME field shown.

B529 (16 May): On 16 May a large swathe of ash was forecast to cover the UK. Peak concentrations of 200- 2000µg/m^3 below altitudes of 6km (< FL200) are shown in the NAME simulation (Figure 1). The aircraft flew over central and northern England, Wales and Scotland and observed ash layers with the lidar between 3 and 6km having concentrations of up to 1000µg/m^3 (Marenco et al., 2011) that is in good agreement with the model. Due to the high concentrations (> 2000 µg/m^3) in the forecast available at the time of the flight the aircraft was not permitted to descend below 6km (FL200). The low concentrations of 20 - 200µg/m^3 shown in Figure 1 over those regions are therefore not representative of peak concentrations; they are merely evidence of "skimming" the tops of those layers. The profile at 1600 – 1630 UTC (Figure 2) over Wales was in largely ash free air just beyond the southern boundary of a large band of high ash concentrations that were observed by the FAAM aircraft lidar (Marenco et al., this issue). In the NAME simulation ash had progressed further south over Wales and Central England (Figure 1) than was observed, either by the FAAM aircraft lidar or satellite imagery.

B530 (17 May): On 17 May the aircraft began from Nantes as it had been re-located at the end of the previous day's flight due to anticipated airspace closures over the UK. The NAME simulation shows a large ash cloud with peak concentrations of 200-2000µg/m^3 between 0 – 6km (0 – FL200) over most of the UK. The early part of flight B530 was conducted at high altitudes (> FL200 ~ 6km) over SE England and other parts of the UK and showed these areas to be free of detectable ash. This confirmed a decision that was made to re-open low-level airspace (< FL200 ~ 6km) on that day. The model error in this case stems from a positional error in a cloud of ash that approached the UK from the North Atlantic on 15 May, as revealed by SEVIRI satellite images (not shown). Directed by satellite imagery some intensive measurements of ash were made over the North Sea during the later part of B530. As shown in Figures 1 & 2 CAS observations of M_{ash} of up to ~500µg/m^3 were encountered during a series of profiles around 54°N, 0 -2°E. A full exploration of those in-situ measurements and the accompanying remote sensing measurements are provided by Turnbull et al. (this issue) and Newman et al. (this issue), respectively.

B531 (18 May): On May 18 the aircraft investigated the edge of an ash cloud travelling down north-eastern parts of the North Sea. No significant ash was observed over eastern England but ash layers were observed over the North Sea by the lidar (see Marenco et al. 2011). In the NAME model some ash was still present over central and eastern parts of England and Scotland due to the earlier positional error that was noted on 16 and 17 May. An intensive pattern of profiles and runs for in-situ and co-located remote sensing was conducted over the North sea. Lower concentrations of ash (maximum ~ 200µg/m^3) were observed compared to the previous day's flight.

5.2 Peak concentrations and column loadings

Ash cloud penetrations have been defined in this study as sections of data where M_{ash} (eqn. 1) exceeded 20µg/m^3 for more than 30 seconds (equivalent to a flight path of ~ 5km). Ash cloud penetrations longer than 10 mins were broken into smaller sections based on indentifying separate layers of ash within the time series. By this definition there were 61 ash plume penetrations from the flights presented in this study (Table 3) but with the bulk of the data from the later flights of B528 – B531 made during 14 – 18 May. Peak concentrations are defined here as the maximum value observed (after 10 second averaging) during an ash plume penetration. Where the ash plume maxima observations were located less than 50km apart only the higher peak value was retained. The range of peak concentrations given in Table 3 is the range of values given by the top 3 peaks per flight. The highest peak values per flight vary from (30 – 4670 µg/m^3) showing the observed variability across this dataset. The ash column loadings have been derived by integrating M_{ash} over the vertical for those profiles that extend

the depth of all ash layers, as can be seen by comparing Figure 2 with Figure 3 of Marenco et al., (this issue). Some flights show very low column loadings of > 0.1 g/m^2 , either where the dominant ash layers were very thin (e.g. B527 on 5 May), where mean concentrations were quite low (B526 on 4 May), or where flight plans led to the avoidance of profiling through any of the thick ash layers (B529 on 16 May). In the case of B521 – B525 (20 – 22 April) all of the above were true.

5.3 Aerosol size distributions
5.3.1 CAS & PCASP

The combined PCASP and CAS (fine and coarse mode) aerosol size distribution is shown in Figure 3, derived using the default processing assumptions (table 2). The plotted lines are the mean distributions for each flight including all ash cloud penetrations. Only bins 2 – 16 of the PCASP are shown, covering the diameter range 0.1 – 0.6μm, to avoid overlap with the CAS instrument (Table 2). The first bin of the PCASP was rejected as it does not have a defined lower boundary as is prone to electronic noise. Only bins 2 – 26 of the CAS are shown, covering volume-equivalent diameters of 0.6 – 35μm. The first CAS bin was rejected as the lower limit of its diameter range was poorly defined and the largest four bins of the CAS (bins 27 – 30) were rejected from the analysis as these returned zero or negligible concentrations in cloud-screened data from ash plumes. The distributions show a fine mode (0.1 – 0.6μm), detected by the PCASP, and a coarse mode (0.6 – 35μm), detected by CAS. The aerosol mass distribution is dominated by the coarse mode (ash) with a peak at around 4μm (volume-equivalent diameter) on all flights. Since the fine-mode is assumed to be accumulation mode aerosol (non-ash) the PCASP data is of little importance in this study; the results are shown here merely to illustrate the distinct separation between the fine and coarse modes at 0.6μm. This means that the CAS instrument alone is sufficient to capture the size range dominated by ash particles. The coarse-mode distributions were fairly well represented by log-normal distributions (Figure 3b); fitting parameters are proposed in (Table 4). As there was some variability in the mean diameter and the width of the coarse mode, three fits are proposed to cover the range of distributions. The middle fit represents an approximate average fit over all flights while the lower and upper fits span the inter-flight variability. Figure 4 shows the variability of effective diameter, D_e (area-weighted mean diameter) and volume-mean diameter, D_v (volume-weighted mean diameter; not the same as d_v, the volume-equivalent spherical diameter) as a function of M_{ash} for all ash cloud penetrations in Figure 4. The data show a weak correlation with M_{ash} and suggest typical values of 1 - 4μm for effective diameter (area-weighted) and 4 - 8μm for volume-mean diameter.

The greatest diameters, broadest size distributions and largest particle sizes (up to $d_v \sim 35$μm) were observed on flight B528 (14May) where the concentrations > 600 μg/m^3 were observed at ~ 700km from the source (compared to more typically distances of 1000 - 1600km from source on other flights). This shows some evidence of sedimentation shaping the size distribution in the distal plume. Variability in the explosive nature of the eruption may also have been important in determining some of the observed variability. Gislason et al. (2011) note the especially high proportion of fine ash (20% mass at grain diameters < 10μm) produced during the initial and most explosive period of the eruption on 14-15 April followed by a change to a coarser (and historically more typical) ash size distribution (<2% mass at grain diameters < 10μm) during a less intensive phase of the eruption on 27 April. The explosive nature of the Eyjafjallajökull eruption re-intensified during May and variability in the volume of glacial ice falling into the eruption crater and in the variability in the intensity of the eruption are likely to have been an influence on the size distribution. These links have not yet been explored and would need a more comprehensive measurement suite than those available on the FAAM aircraft platform.

The CAS size distributions differ significantly from the measurements of Schumann et al. (2011) where the volume peak is shown at 8 - 10µm. Turnbull et al. (this issue) show that this discrepancy is not related to differences in assumed refractive index or particle shape but more likely related to uncertainties in instrument performance. The in-situ measurements made at the Jungfraujoch high-altitude research station (3580m a. s. l.) gave volume peaks at diameters of around 3µm (Bukowiecki et al., 2011); slightly smaller than in our results where CAS mass peaked at diameters of around 4µm (Figure 3). This is not surprisingly, given that their observations were made further downwind than ours and therefore affected by further size-selective sedimentation. Some support for the CAS size distribution is also provided by the successful longwave and shortwave radiative closure in Newman et al. (this issue). In-situ observations of airborne ash from past eruptions are limited. Aircraft observations following the eruptions of Mt. St. Helens and Mt. Redoubt (Hobbs et al., 1982; Hobbs et al., 1991) showed ash volume modes peaks between 10 – 30µm but at close distances to source (10 – 170km). Analysis of surface deposits from the Shetland Isles (60°N, 1°W) (SEPA 2010) showed evidence of some glassy shards with dimensions of 15 – 45µm following the mid-April phase of the eruption. An exceptional shard of 30µm width and 188µm length was also found within the sample; these shards would likely shatter to form fragments if sampled by the aircraft instrumentation.

These results can be used to refine the distribution of ash particle sizes released in dispersion models. For example, the size distribution assumed in NAME is from Mount Redoubt, St Augustine and Mount St Helens as presented by Hobbs et al. (1991), and has a peak for diameters between 10 – 30 µm, with 75% of the mass at diameters > 10µm. This contrasts against the CAS results where typically less than 10% of the mass was in the size range d_v > 10µm. However, one can not make a direct comparison of emitted size distributions with those observations downwind owing to size-selective processes such as gravitational settling and deposition that shape the size distribution over time. NAME simulations in Devenish et al. (this issue) indicate that fall out begins to have a strong affect on modelled mass concentrations in downwind regions when a large portion of the modelled ash is associated with particle diameters > 15 - 20µm. The CAS observations in Figure 3 suggest that this drop-out may dominate for d_v > 10µm. Millington et al. [2011] also provide some indication that the NAME emitted size distribution is not in line with observations downwind from the volcano. In their work simulated SEVIRI BT10.8-BT12.0 and dust RGB satellite images better matched the real satellite images when the simulated size distribution for the ash had reduced particle sizes (peak at 5µm), compared to emitted size distribution assumed in NAME (peak at 20 microns). In further work, it would be interesting to compare the NAME downwind size distribution with that observed and used to provide the best simulated satellite imagery. Some work has already been carried out comparing NAME particle size distributions downwind with the FAAM observations (Helen Dacre, personal communication). Results show that NAME requires a modified effective source particle size distribution, containing a larger fraction of sub 10um diameter particles than described above, to capture the particle size distribution derived from the CAS measurements presented here. This is consistent with the idea that Eyjafjallajokull emitted very fine particles due to the interaction of volcanic ash with the ice cap (Gislansona et al. 2011). However, one can not generalise this conclusion to all eruptions as effective source particle size distributions vary.

5.3.2 SEM analysis

The CAS size distribution has also been compared to sizing results from SEM analysis of ash samples collected on filters during flight. Figure 5 compare flight averaged size distributions for flights B530 and B531 (17 & 18 May) on which the duration of in-situ sampling and filter exposure led to both favourable filter loadings and good particle counting statistics. For flight B530 (17 May), 4585 particles were individually analysed from the 1µm filter and 6707 particles on the 10µm filter (310 fields of view) compared to 8273 particles from 100 fields of view from the 10µm filter collected on flight B531 (18 May). These filters had been exposed

continuously during all parts of the flights when ash in-situ sampling occurred and therefore represent a flight mean.

The SEM analysed size distributions are compared against the flight mean size distribution from CAS (Figure 5). Both CAS and SEM size distributions have been normalized to give a volume of unity when integrating dV/dlogD over the $1 - 15\mu m$ diameter range to allow a comparison of size distribution shape rather than absolute concentrations. The agreement is remarkably good despite fundamental differences in the ways that d_v are derived. In the SEM analysis d_v is assumed to be equal to d_a, the diameter of a sphere of equivalent cross-sectional area. This may greatly overestimate the volume of particles with large aspect ratio, especially if those particles preferentially lie flat on the filter exposing their maximum cross-sectional area. The size range provided by the SEM analysis is more limited than that of CAS. Particles smaller than $1\mu m$ are not all retained due to the $1\mu m$ pore size whereas particles larger than $10\mu m$ may be under-sampled due to impaction within the inlet and sample pipes. This may explain the tail off in the SEM size distribution for $d_v > 10\mu m$, and the lack of particles for $d_v > 15\mu m$. Thus the observed SEM size distribution is to some extent a reflection of the collection efficiency of the filter system and the apparent agreement with CAS may be somewhat fortuitous. Nevertheless, some confirmation of ash volume peaking around $4\mu m$ can be drawn from the comparison.

5.3.3 AERONET
The flight mean PCASP and CAS size distribution from flight B530 (17 May) has also been compared to size distribution retrievals from AERONET sunphotometers (Fig 6). The sites of Helgoland (54.2°N, 7.9°E), Brussels (50.8°N, 4.3°E), and Cabauw (52.0°N, 4.9°E) were selected for the period from 1500UTC on 17 May to 1800UTC on 18 May as NAME back trajectories (not shown) and satellite imagery (Newman et al., this issue) showed that, during this period, these sites were affected by the same ash cloud that the FAAM aircraft observed in the southern North Sea on 17 May (Figure 1). These retrievals showed strong indicators of ash including increases in coarse-mode AOD from values of ~0.05 to values of ~0.2, and the increased dominance of the coarse-mode (typically diameters of $0.6 - 30\mu m$) in the volume size distributions (Fig 6), compared to retrievals from previous or later days in May 2010.

The plotted lines in Figure 6 are normalized by coarse-mode volume ($d > 0.6\mu m$) to focus the comparison on this part of the size range where ash is assumed to dominate. The site mean AERONET retrievals are similar across the three sites peaking at $3 - 4\mu m$. These show remarkably good agreement with the FAAM aircraft measurements in both the peak (~$4\mu m$) and width or the coarse-mode. This shows an encouraging level of consistency between the CAS in-situ measurements and the retrievals based on observed sky radiances. As the AERONET retrievals are sensitive to the whole aerosol column they exhibit large fine modes ($0.2 - 0.3\mu m$) that are likely to be dominated by boundary layer aerosol, which is probably of non-volcanic origin (see Turnbull et al., this issue). The FAAM aircraft data did not include sampling in the boundary layer and this may explain the comparatively small fine mode.

5.4 Ash particle shape
The shape of aerosol particles has important influence on the scattering response in optical particle counters and therefore the derived particle size and mass. Therefore, the study of ash particle shape is an important area of research and is examined from both SEM images and from scattering patterns detected by the SID-2H instrument.

5.4.1 SEM images
Due to the explosive nature of the eruption the ash from Eyjafjallajökull had highly irregular non-spherical shapes including angular crystalline structures, aggregates and sharp glassy shards (Schumann et al., 2011; Bukowiecki et al., 2011; Pyle et al., this issue; Gislason et al.,

2011). Figure 7 shows example Scanning Electron Microscope (SEM) images, taken from ash collected on the FAAM aircraft filter system during flights B530 and B531 (17 & 18 May). These images demonstrate the non-spherical nature of the ash and the need for more complex treatments of irregularly-shaped particles within optical scattering models (section 4.2). Gislason et al. (2011) show that the ash produced during the initial explosive phase on 14 -15 April and deposited ~55km from the crater was especially fine-grained with sharp edges and rough surfaces, even at sub-micron scales. Another near-source deposit collected on 27 April when the eruption was less explosive contained larger ash particles that were considered more typical based on previous studies from other volcanoes (Gislason et al., 2011).

5.4.2 SID-2H scattering patterns
The highly irregular shapes of ash were also evident on examining forward scattering patterns on the SID-2H instrument. A selection of SID-2H scattering patterns is shown in Figure 8 taken from the same ash layer observed during flight B526 (4 May). Each image is a polar plot related to the azimuthal variation of scattered light intensity; the plot radius for each photodetector element is approximately proportional to the square root of detector response (and therefore scattered light amplitude). Hence plot area is proportional to particle cross sectional area and for spherical particles (with uniform azimuthal response) plot radius is proportional to particle radius. The asphericity factor (A_f), as original devised by Hirst et al. (2001) is a unitless quantity varying from $0 - 100$ that is proportional to the standard deviation in scattered intensity amongst the azimuthally arranged detectors. The asphericity factor gives an indication of how far the particle's shape is from spherical; it is defined as:

$$A_f = \frac{k\sqrt{\sum_i^n (\overline{S} - S_i)^2}}{\overline{S}} \qquad (4)$$

Where S_i is the ith detector element response out of $n = 28$ azimuthally arranged detectors and $k = 3.64$ is a constant so that $0 < A_f < 100$.

The scattering patterns from the ash layer (Figure 8b) exhibit high variability in the scattering amplitude with azimuthal angle, evidence of non-spherical shapes with high aspect ratios and smooth facet-like surfaces (Ulanowski and Schnaiter 2011). These highly non-spherical particles are detected for nominal diameters of ~0.5 – 6µm. These contrast against the almost uniform scattering patterns (Figure 8a) from aerosol sampled during a 30m run over the Irish Sea earlier in the flight. The spherical aerosol in Figure 8a is in general larger than the non-spherical ash of Figure 8b with nominal diameters of 3 – 12µm. The spherical nature of the low-level aerosol may be taken as evidence of liquid and due to the location of these measurements we assume the aerosol to be hydrated sea-salt. As illustrated the SID-2H is therefore a useful tool in discriminating between particle types and was used to reject CAS data suspected to be hydrated sea-salt during low-altitude (< 300m) sections of flight over the sea on flights B526 (4 May) and B531 (18 May). In the absence of such information hydrated sea-salt that had mass concentrations of ~200µg/m³, as detected by CAS, may have been misdiagnosed as being predominantly ash.

Laboratory investigations (results not shown) indicate that the ratios between forward and back scattering, and depolarized back scattering signal provided by the CAS could be used to discriminate between spherical and non-spherical particles, and possibly even distinguish between ice and ash particles. The discrimination between ash and ice with SID-2H light scattering patterns may also be possible though difficult as the light scattering patterns from ash appear similar to some obtained from small ice particles (Cotton et al. 2010), even though the asphericity factor appears to be somewhat higher for ash than for ice. This surprising finding could be a consequence of the angular but smooth shape of the ash particles, as evidenced by the SEM images. In contrast, flight data from the high-resolution SID3 probe obtained in a variety of ice containing clouds shows predominantly scattering patterns with very fine, speckly structure, interpreted as being due to the dominance of particles with irregular and/or rough surfaces (Ulanowski et al. 2010). Such patterns lead to relatively high

azimuthal uniformity, when seen by the SID-2H probe. More pristine, smooth ice crystals on the other hand produce highly non-uniform patterns (Ulanowski et al. 2006) and such crystals could be confused with the type of ash particle seen in this study, making it difficult to discriminate solely on the basis of low-resolution azimuthal scattering patterns.

5.5 Uncertainties in CAS derived size distribution and mass concentration
5.5.1 Sensitivity to refractive index and particle shape assumptions
Figure 9 shows the scattering cross-section of ash particles, integrated across the angular range detected by CAS ($4 - 12^o$), for the three cases (see Table 2), as a function of d_v. The instrument response for water spheres was also calculated (Figure 9) for reference, as this corresponds to the nominal (uncorrected) bin diameters. These curves are used to estimate the minimum and maximum d_v for each of the 30 size bins, according to the range of scattering amplitudes associated with each bin. On average the scattering amplitude from the irregular ash treatment is not far from the scattering amplitude predicted for water spheres. This occurs due to the cancellation between opposing effects of increased particle cross-sectional area per unit volume (resulting in higher specific extinction, k_{ext}), versus increased absorption, and a decreased preference for forward scattering. This approximate cancellation means that the derived bin diameters (d_v) for the default case (labelled as "ash irregular" in Figure 10) are not far from the bin diameters that would be given for water, producing similar size distributions and mass concentrations. However, the spherical ash treatments lead to significantly lower scattering amplitudes as a function of d_v, mainly due to decreased extinction cross-section of spheres compared to irregular shapes. The increase in the imaginary part of refractive index in the more absorbing ash sphere case further decreases the scattering cross-section for $d_v >$ ~10μm. The spherical ash treatments lead to higher derived values of d_v for the CAS bins particularly in the upper part of the size range ($d_v > 10$μm), a much broader coarse mode and greatly increased M_{ash} (Figure 10).

The example shown in Figure 10 (ash plume encountered at 60^oN, 7^oW on flight B528, 14 May) demonstrates the sensitivity of M_{ash} to these assumptions. The assumption of spheres increases the mean M_{ash} by 24% and increases the maximum M_{ash} by 32%, compared to the default (irregulars) case. The assumption of more absorbing spheres increases the mean M_{ash} by 65% and increases the maximum M_{ash} by 83%, compared to the irregular case. This means the increase of refractive index alone increases mean and maximum M_{ash} by 33% and 39% in the spherical case. In other sections of data, particularly data samples with fewer large particles (e.g. B526 on 4 May), the sensitivity to these assumptions was lower; the example shown in Figure 10 demonstrates the highest sensitivity that was found from all ash flights due to it having the highest proportion of particles above 5μm. However, as a demonstration of the maximum sensitivity, and treating the assumptions of refractive index and shape independently, the results above suggests a maximum uncertainty of up to 50% (or a factor of 1.5) in peak values of M_{ash}. The impact of the correction for gain stage overlap can be seen by contrasting the "uncalibrated" and "water" results in Figure 10. The correction delivers a smoother and more monotonic size distribution and increases M_{ash} by ~60%.

5.5.2 Uncertainty introduced by ice clouds
The uncertainty introduced by ice cloud is illustrated in Figure 11. In this profile on 14 May, the aircraft descends through a layer in which the relative humidity is close to or just above saturation with respect to ice. The extreme mass concentrations indicated in the unscreened CAS data are well correlated with peaks in ice water content (IWC) derived from the CIP-15. It is reasonable to assume that these extreme values result from the detection of cloud ice particles by the CAS, possibly enhanced by shattering of the ice on the CAS intake tube. The discrepancy in IWC measured by the CIP-15 and Nevzorov probe results in part from the tendency of ice particles to rebound from the Nevzorov collector reducing the measured IWC below the true value (A.Korolev, personal communication).

In this profile descent, the highest screened value of M_{ash} of 4670 µg/m^3 occurs at 6800m altitude, below the lowest altitude at which the CIP-15 detects ice particles and where the relative humidity with respect to ice has fallen to around 80%. It is reasonable to assume that these values are not directly influenced by the presence of ice particles. Nevertheless, this region has an anomalously high ratio of M_{ash} (4670 µg/m^3) to nephelometer-derived aerosol scattering at 550nm (~520 Mm^{-1}); a ratio of ~9 g/m^2 compared with more typical ratio of 3 g/m^2 (see Figure 13b). Also, Lidar estimates of the peak ash mass (based on aerosol extinction) reach only 1900µg/m^3 (Marenco et al., this issue). This inferred increase in the ratio of mass to scattering or extinction is not supported by the CAS size distribution that differs only marginally between this section of data and data from other flights (Figure 3b). With the presently available data, it is not possible to explain this apparent discrepancy. It may, however, be related to characteristics of the ash particles generated by previous physical processing within cloud. For example, they may retain partial ice coatings or their aggregation state may have been modified, generating changes in their physical and optical properties. We suspect the screened CAS peak value in this profile to be an overestimate but further research is necessary to explore methods of distinguishing these kinds of problems.

5.5.3 Overall uncertainty in mass concentration

The main sources of uncertainty in the estimation of M_{ash} are:

1) Uncertainty in sizing accuracy due to the limitations of the calibration procedure, including corrections for increased gain stage overlap. This is estimated as a factor of 1.5 (equivalent to a 15% error in diameter, the typical diameter difference between neighbouring bins).

2) Uncertainty in particle sizing due to uncertainties in refractive index and particle shape. This is estimated as a factor of 1.5, based on independently considering the contrast between spheres and irregulars, and spherical calculations varying the refractive index real part from the default value of $1.52 + 0.0015i$ to $1.59 + 0.004i$ (section 5.5.2).

3) Uncertainty in particle concentrations due to uncertainty in the optical cross-section (0.24mm^2) of CAS and the measured air-speed (and its variation between the nose and the position of the CAS probe under the wing). This is estimated as a factor of 1.3.

4) Uncertainty in the density of volcanic ash. Based on the recent literature and the possibility of inclusion of voids, an uncertainty of +/-500 kg /m^3 or ~20% seems reasonable.

Assuming these errors to be independent, a root sum of log squares approach gives an overall uncertainty of a factor of 2. Given that uncertainties relating to particle properties (refractive index, shape, and density) could be interdependent it is conceivable that errors of greater than a factor of 2 could occur. However, since such interdependencies are not known, the factor of 2 uncertainty, based on assuming independent errors, can be viewed as a suitable guide to the overall uncertainty. Additional un-quantified sources of error may exist including:

1) Particle shattering on the instrument tip or turbulent break up of micro-aggregates.

2) Air bubbles within ash particles and aggregations of particles that could substantially reduce density to values, potentially below the lower limit we assume (2300 +/- 500 kg/m^3 gives a lower limit of 1800 kg /m^3) and alter scattering properties.

3) Coatings of secondary aerosol material (e.g. Schumann et al., 2011), water or ice on ash particles, amplifying the scattering signal and derived mass.

4) Contribution to the coarse-mode from externally mixed small ice particles (nominal diameter < 30µm) that may have been present but undetected beneath or adjacent to cirrus cloud.

5.6 Correlation of ash mass with aerosol scattering and SO$_2$

5.6.1 Vertical profiles

The patchy and inhomogeneous nature of distal ash clouds is commonly seen in satellite imagery and airborne lidar cross-sections (Francis et al., this issue; Millington et al., this issue; Marenco et al., this issue; Schuman et al., 2011; Royer et al., 2011). The vertical profiles of Figure 12 show representative examples of the vertical distribution of ash (M$_{ash}$, lidar-derived ash mass, nephelometer scattering coefiicients), and SO$_2$ observed during the FAAM aircraft flights. Figure 12 shows that the ash layers (defined as > 20μg/m^3) range in depth from 500m to 2km and show a large degree of internal variation. The vertical distribution of the aerosol scattering, and SO$_2$ concentration appear correlated with M$_{ash}$. Since the aircraft profiles cover a horizontal distance of ~25-30km for every km they ascend or descend some of the variability in the in-situ profiles is also linked to horizontal inhomogeneity. Figure 11 also shows retrievals of ash mass concentration from the airborne lidar (Marenco et al., this issue), taken at high altitude just before the aircraft descents, or after the ascents. The lidar retrievals are averaged over only 8 – 10 km in the horizontal. They show the same kind of vertical depth for the ash layers as the in-situ measurements. Magnitudes of lidar-derived ash mass concentration are also similar to M$_{ash}$, as found in Marenco et al. (this issue) and Turnbull et al. (this issue). This small-scale vertical variability could lead to wholly different outcomes for aircraft encountering the same ash cloud at different altitudes or flight trajectories. Moreover, this shows the difficulty of interpreting the outcomes of un-instrumented test flights. The profiles show strong correlations between M$_{ash}$, nephelometer scattering coefficient and SO$_2$ concentration, except below 1 or 2km where fine boundary layer aerosol gives rise to increased nephelometer scattering. Some sections of CAS data below 2km are missing from these profiles due to the rejection of data affected by water cloud (appendix B) or sea-salt (see section 5.4.2) or other aerosol prevalent to the atmospheric boundary layer aerosol. Significant concentrations of ash (M$_{ash}$ > 200μg/m^3) were not observed in the atmospheric boundary layer on any of the flights. This may be in part due to the altitude and advection from the source or the result of wet and dry removal processes in the boundary layer.

5.6.2 Variability from ash cloud penetrations

The variability and correlations between M$_{ash}$, SO$_2$ and nephelometer scattering is examined from all ash cloud penetrations in Figure 13. Figure 13a shows that peak ash concentrations were typically 2 or 3 times greater than mean concentration during ash cloud penetrations but in some cases 5 times greater. This highlights the difficulty of comparing peak and mean values amongst observing systems and models that involve differing spatial and temporal scales. The extreme inhomogeneity highlights just how difficult it is to target (or conversely avoid) the most dense ash patches with aircraft. It also shows that it is right to allow for a substantial peak-to-mean ratio in models such as NAME where computational constraints and incomplete knowledge of the rapidly fluctuating ash source term limit the temporal and spatial resolution of ash dispersion.

The ratio of nephelometer scattering to M$_{ash}$ varied from 0.1 to 1.0 m^2/g, with the lower ratios occurring on flight B528 (14 May) and the higher ratios occurring on flight B526 (4 May). The linear best fit suggests a typical ratio of 0.3 m^2/g for M$_{ash}$ > 200 μg/m^3. This ratio should not be interpreted as a direct estimate for specific scattering coefficient (k$_{sca}$) as the Rosemount inlet serving the nephelometer is not designed for sampling coarse particles and may under-sample the coarse mode. However, the nephelometer-implied k$_{sca}$ values are of similar magnitude to the k$_{ext}$ estimates in Table 5 and Figure 14 showing that the issues of light-absorption and inefficient sampling of coarse particles do not prevent the nephelometer from serving as a useful guide or constraint to ash mass concentrations. Moreover, as heating inside the cabin and the nephelometer instrument removes water or ice from the aerosol sample the ratio of nephelometer scattering to M$_{ash}$ can be used to aid the discrimination between ash and water or ice clouds in the interpretation of coarse-particle optical particle

counter data. However, caution should be taken applying these k_{ext} estimates to other volcanic ash scenarios; if the mass associated with large particles (e.g. $d_v > 10\mu m$) was much larger than in these FAAM observations then the correspondence between the nephelometer scattering and M_{ash} may break down.

The Angstrom exponent derived from the nephelometer, via the ratio of red (450nm) and blue (700nm) aerosol scattering coefficients, was anti-correlated with M_{ash} (Figure 13d) decreasing from values of 1.0 - 1.3 in plumes of low mean ash concentration ($> 30\mu g/m^3$) to -0.4 – 0.1 in plumes with mean $M_{ash} > 200\mu g/m^3$. The Angstrom exponent depends on the aerosol size distribution, generally decreasing with increasing particle diameter. Typical values are 2 for urban aerosol, 1-2 for rural haze, and 0 for coarse aerosol [Baltensperger et al., 2003]. The relationship in Figure 13d can therefore be explained as evidence of an increasing dominance of coarse aerosol as M_{ash} increases. The Angstrom exponent is therefore shown to be a useful diagnostic for the identification of ash layers (Hogan et al., this issue). Mie calculations with the observed size distributions and a range of spectrally varying refractive index assumptions (based on literature sources cited in section 4.2) do not produce Angstrom exponents lower than -0.2, and can not explain the very low values of -0.4 derived from the nephelometer. This discrepancy has not been resolved but it may suggest a low bias in the blue or a high bias in the red channels, or biases in both, resulting in an underestimation of up to 10% in the ratio between the blue and red scattering.

The concentration of SO_2 was in general well correlated with M_{ash} on any particular flight (Figure 13c & Figure 12) as also found by Turnbull et al. (this issue) and Schuman et al. (2011). However, the exact ratio between SO_2 concentration and M_{ash} shows a large degree of variability between flights and some variability between different profiles on the same flight. A notable outlier is flight B526 (4 May) where SO_2-rich layers were observed sometimes with a relatively small coarse mode compared to other flights (Figure 3) and non-depolarizing particles in lidar returns (Marenco et al., this issue). These measurements suggest widely varying fine ash / SO_2 emission rates from the eruption, or the large differences in the time-evolution of physical and chemical processes affecting the concentrations of ash and SO_2 in plumes. Excluding flight B526 (4 May) the ratio of SO_2 to M_{ash} ranges from 30 to 250ppbv per $1000\mu g/m^3$, similar to the range of 50 – 350 ppbv per 1000 $\mu g/m^3$ suggested by Figure 26 of Schuman et al. (2011). The results indicate that although SO_2 is a useful tracer of volcanic emissions for these flights it does not provide a reliable indicator or constraint on likely ash concentrations. As noted elsewhere (e.g. Thomas and Prata 2011) ash and SO_2 layers are not always co-located.

5.7 Specific extinction coefficient

The specific extinction coefficient is a parameter of particular interest as it relates the mass of aerosol to the optical extinction, which may be derived from remote sensing retrievals such as those based on lidar, sunphotometer and satellite data:

$$M_{RS} = 10^6 (f_c \sigma / k_{ext}) \tag{2}$$

where M_{RS} is the ash mass concentration ($\mu g/m^3$) derived from a remote sensing method, σ is the aerosol extinction coefficient (m^{-1}), f_c is the fraction of aerosol extinction associated with the coarse-mode (i.e. the ash), and k_{ext} is the coarse-mode specific extinction coefficient (m^2/g). In general terms the specific extinction coefficient is a parameter expressing the extinction cross-section of the aerosol population (m^2) divided by its mass (g). In this study k_{ext} is derived from CAS in the following way:

$$K_{ext} = \frac{\sum_{i=2}^{26} N_i Q_{ext,i} \pi r_a^2}{\left(M_{ash} / 10^6 \right)} \tag{3}$$

where N_i is the number concentration (m^{-3}) in size bin i of the CAS instrument spanning bins 2 – 26 (see section 4.1), $Q_{ext,i}$ is the unit-less extinction efficiency (extinction cross-section / physical cross-section area), r_a is the area-equivalent radius (the radius of a sphere with the same physical cross-section as the given irregularly-shaped particle). M_{ash} is the ash mass concentration estimated from CAS, as defined in equation 1. Q_{ext} was calculated for the median diameter of each CAS size bin from the optical scattering models, assuming default processing assumptions (Table 2). Mean values of k_{ext} for each flight are also shown in Table 5 for wavelengths (λ) of 355nm (for application to the on-board lidar), 550nm (nephelometer green channel wavelength) and 680nm (CAS laser wavelength). On most flights the coarse mode dominated the optical extinction in ash clouds whereas on flight B526 (4 May) the k_{ext} estimates are higher due to the influence of the fine mode of secondary aerosol. The coarse-mode k_{ext} is therefore a more reliable quantity to apply in situations of high ash concentration. Coarse-mode k_{ext} results for 550nm are also shown for each of the 55 ash cloud penetrations of flights B526-B531 (4 – 18 May) in Figure 14; values vary from 0.45 to 1.06 m^2/g. The upper estimates from flight B526 are somewhat outliers and indicate different aerosol characteristics on this case. Marenco et al. (this issue) also note the different aerosol properties in lidar returns on B526 (4 May) where some of the elevated aerosol layers were non-depolarizing (indicating a greater influence of spherical particles, i.e. secondary aerosol). The lower estimates of coarse-mode k_{ext} are from the section of flight B528 (14 May) to the north-west of Scotland (Figure 14), where larger ash particles (20 – 35 μm) were observed.

The data in Figure 14 suggest a representative value for k_{ext} of 0.6 m^2/g may be appropriate, based on the convergence towards this value in the upper range of the observed concentrations (> 600 μg/m^3). As shown in Table 5 this estimate could be applied across any UV – visible wavelengths as the coarse mode k_{ext} results are relatively insensitive to wavelength. This was linked to the dominance of coarse particles ($d_v \gg \lambda$) and not greatly influenced by the variation (or lack of variation) of refractive index with λ. For comparison k_{ext} was also derived for the log-normal fits of Figure 3b (Table 4) and gave a range of 0.57 – 0.77, with a best estimate of 0.66 m^2/g when integrated with the irregular ash optical properties (Table 6). The application of Mie theory led to slightly lower k_{ext} estimates (range of 0.41 – 0.59 m^2/g and "best estimate" from log-normal fits was 0.49 m^2/g) showing a modest sensitivity to particle shape assumption.

Other estimates of ash k_{ext} for Eyjafjallajökull are provided in Table 6. All values in this table have been adjusted, where necessary, for the density assumed in this study (ρ_{ash} = 2300 kg/m^3) to allow side-by-side comparison. Ansmann et al. (2010) assume k_{ext} of 0.51 m^2/g (for 355 and 532nm) based on the desert dust size distributions of the OPAC (Optical Properties of Aerosols and Clouds) [Hess et al., 1998] data base. This was used to derive mass estimates of 1000μg/m^3 from the combination of Raman lidar (as part of the European Aerosol Research Lidar Network, EARLINET) and AERONET sunphotometer at Leipzig. Their k_{ext} estimate is equivalent to 0.58 m^2/g when adjusting to our assumed density of 2300 kg/m^3. Hogan et al. (in prep.) estimate k_{ext} of 0.84 +/- 0.28 m^2/g at 355nm based on constraining a model of ash particles to fit lidar and sunphotometer measurements at Chilbolton (Southern England) on 16th April. Assuming a density of 2300 kg/m^3 yields 0.95 m^2/g for the Hogan et al. data and methodology. Their ash model was a log-normal distribution of glassy particles with median diameter of 3.7μm and standard deviation of 2.2, based on an internal mixture of 75% mineral (RI = 1.56 + 0.005i) and 25% air. We derive a k_{ext} estimate of 0.25 m^2/g from the ash data collected by the DLR Falcon aircraft (Schumann et al. 2011). This was derived by fitting a log-normal to the coarse mode size distribution gathered from the PCASP, GRIMM OPC (Optical Particle Counter) and FSSP (Forward Scattering Spectrometer Probe) instruments of the Falcon during their North Sea flight on 17 May (see Turnbull et al., this issue) and applying Mie theory using the refractive index from Schumann et al.'s medium absorption assumption (1.59 + 0.004i), along with our density assumption of 2300 kg/m^3. Applying the same log-normal fit and density to the irregular ash shape model used in this study and our default refractive index (1.52 + 0.0015i) provides a k_{ext} estimate of 0.36 m^2/g.

The above comparisons suggest a specific extinction coefficient of 0.6m^2/g to be a reasonable best estimate for distal ash clouds (~1000km or more downwind) from the Eyjafjallajökull eruption, with a maximum uncertainty of a factor of 2 based on the full range of estimates above. This includes variability between the April and May periods of eruption.

6. Conclusions

In-situ measurements of volcanic ash particles were made by the FAAM aircraft during a series of flights in April and May 2010. This opportunistic, and difficult to obtain dataset adds substantially to the limited set of in-situ observations of volcanic ash properties. The observations show strong evidence of volcanic ash clouds over the UK and surrounding regions during April and May 2010, following the eruption of Eyjafjallajökull. Owing to safety policy, in-situ sampling was obtained by profiling through ash layers in regions forecast to have concentrations less than 2000μg/m^3. Ash mass concentrations derived from the CAS instrument (M_{ash}) peaked in the range 20 – 60 μg/m^3 for the flights on 21 and 22nd April and in the range 100 – 600 μg/m^3 for the flights on 4, 5, 16, 17 and 18 May, with a factor of 2 uncertainty. The ash was mainly found between altitudes of 2 – 6 km. The peak values of 100 - 600μg/m^3 observed during the May flights were pre-dominantly in regions predicted to have ash mass concentrations in the range 200 - 2000μg/m^3, showing that the NAME dispersion model generally predicted the appropriate magnitude of ash concentrations in downwind regions (1000 – 2000km from the volcano). On 14 May higher values of M_{ash} in the range 2000 – 5000 μg/m^3 were observed briefly (for four minutes) at altitudes of 6 – 8km over the south-west of Scotland, exceeding the forecast range. However, these are suspected to have been overestimates due to possible mixing of ash with ice. Although no damage to the aircraft was noted on post-flight inspections, given the short exposure (four minute) to concentrations above 2000μg/m^3, and the uncertainty in these peak estimates, no conclusions about the appropriateness of aircraft safety limits can be made from this flight.

The size distribution from the CAS showed a coarse mode with volume equivalent diameters (d_v) ranging from 0.6 – 35μm, although the majority of M_{ash} (~90%) was from particles with d_v in the range 1 - 10μm. The flight-averaged mass distributions peaked at d_v between 3 – 5μm and there was a rapid fall off beyond 10μm. These were remarkably similar to the size distributions obtained from SEM analysis of samples collected from the on-board filter system. The agreement with AERONET size distribution retrievals is also encouraging. The application of light-scattering models to the CAS size distributions suggest specific extinction coefficient (k_{ext}) of the ash aerosol in the range 0.45 – 1.06 m^2/g, with a typical value of 0.6m^2/g in ash-dominated aerosol samples. These estimates of k_{ext} are unlikely to be representative of near-source properties (e.g. < 100km) but may provide a guide for the properties of distal ash clouds in future eruption scenarios, and for application to satellite products and other remote sensing retrievals.

SEM images of ash and scattering measurements from the Small Ice Detector (SID2H) showed a high degree of asphericity, irregularity and diversity in ash particle shapes. This asphericity was an important feature enabling the use of SID-2H data to discriminate ash from hydrated sea-salt that gave more symmetric scattering patterns. Particle shape was a significant source of uncertainty (~25%) in estimating the volume, and M_{ash}. The refractive index assumption was another strong source of uncertainty (~35%) in M_{ash}. The combination of these, and other uncertainties in ash particle properties (aggregation and internal mixing), plus instrumental sources of uncertainty lead to a factor of two uncertainty in M_{ash}. Additional sources of uncertainty include the mixing of ash with ice during the flight on 14 May.

The measurement of aerosol scattering coefficient at multiple wavelengths was shown to be a useful accompaniment to ash mass concentration estimates from optical particle counters such

as CAS. High aerosol scattering coefficients and low Angstrom exponents were well correlated with M_{ash}. Therefore, by using a-priori estimates of k_{ext}, minus a correction for absorption, aerosol scattering can serve as a rough guide to ash concentration. At very least this information provides confirmation of coarse aerosol, aiding the discrimination between ash and water or ice cloud. Significant concentrations of ash (> 200 μg/m^3) on these flights were always accompanied by elevated levels of SO_2 (5 - 100ppbv above background levels) but the ratio between M_{ash} and SO_2 varied by more than an order of magnitude. Also, on 4 May moderate elevations of SO_2 (e.g. 10ppbv) were observed in ash-free aerosol layers of the mid-troposphere. Such layers contained a greater proportion of fine aerosol (d < 0.6μm) that was assumed to be sulphuric acid and/or sulphate.

Changes in the explosive nature of the eruption between April and May mean that our observations may not necessarily reflect the properties of ash that affected Europe during 15 - 22 April. However, the results from AERONET and the Jungfraujoch research station suggest similar particle size distributions during the April and May phases of the eruption, at least for the component of the ash distribution that is transported over great distances (> 1000km) downwind. Therefore, many of the conclusions may hold in general within the context of the 2010 eruption of Eyjafjallajökull. Whether these conclusions can be applied to other eruptions is a more open question. The very fine nature of the Eyjafjallajökull ash, relative to ash particle sizes observed from past eruptions, has been related to the explosive, phreatomagmatic nature of the eruption (Gislason et al. 2011) and its light colour has been related to the high silica composition (Schumann et al., 2011). This contrasts against more basaltic eruptions (e.g. Grimsvotn May 2011) that produce coarser grains and visibly darker ash deposits. Further research is required to understand what determines the composition, and the physical and optical properties of ash. Can these be linked in a quantitative way to known characteristics of volcanoes, or observable features of eruptions? Initial results suggest that the Eyjafjallajökull 2010 eruption produced much finer ash than assumed in the NAME model. However, this discrepancy has not been fully explored and may be a consequence of eruption characteristics that could not have been predicted in advance.

The scattering of light by irregularly shaped ash particles is also poorly understood due to the extreme complexity and variability of particle shapes. Experimental analysis of the scattering phase functions of ash particles is therefore required to test theoretical models, such as the application of ray-tracing methods to polyhedral crystals, as used in this study. Improvements to optical particle counter techniques, including calibration and data interpretation methods for complex particles of irregular shapes and mixed composition are also topics for future research. The examination of backscattering and depolarization measurements from instruments such as CAS may also lead to techniques for discriminating between ash, ice and other coarse aerosol.

Acknowledgements

References

Anderson, T. L., J. A. Ogren (1998). Determining aerosol radiative properties using the TSI 3563 Integrating Nephelometer, *Aerosol Sci. Technol.*, 29, 57–69.

Andreae, M. O., H. Berresheim, T. W. Andreae, M. A. Kritz, T. S. Bates, and J. T. Merrill (1988), Vertical distribution of dimethylsulfide, sulphur dioxide, aerosol ions, and radon over the northeast Pacific Ocean, *J. Atmos. Chem., 6*, 149– 173, doi:10.1007/BF00048337.

Ansmann A., M. Tesche, S. Groß, V. Freudenthaler, P. Seifert, A. Hiebsch, J. Schmidt, U. Wandinger,I. Mattis, D. Muller, and M. Wiegner (2010), The 16 April 2010 major volcanic ash plume over central Europe: EARLINET lidar and AERONET photometer observations at Leipzig and Munich Germany, *Geophys. Res. Let,,. 37*, L13810 doi:10.1029/2010GL043809.

Balkanski, Y., M. Schulz, T. Claquin and S. Guibert (2007), Reevaluation of mineral aerosol radiative forcings suggests a better agreement with satellite and AERONET data, *Atmos. Chem. Phys.*, *7*, 81-95.

Baltensperger, U., S. Nyeki, and M. Kalberer (2003), Atmospheric particulate matter, in Handbook of Atmospheric Science, edited by C. N. Hewitt and A. Jackson, pp. 228-254, Blackwell, Malden, Mass.

Baran, A. (this issue), A new application of a multi-frequency submillimetre radiometer in determining the microphysical and macrophysical properties of volcanic plumes: A sensitivity study, *submitted to J. Geophys. Res.*

Baumgardner D., H. Jonsson, W. Dawson, D. O'Connor, and R. Newton (2001), The cloud, aerosol and precipitation spectrometer; a new instrument for cloud investigations, *Atmos. Meas. 59-60*, 251-264.

Brown, Philip R. A., Peter N. Francis, (1995) Improved Measurements of the Ice Water Content in Cirrus Using a Total-Water Probe. *J. Atmos. Oceanic Technol.*, **12**, 410–414.

Bukowiecki, N., P. Zieger, E. Weingartner, Z. Jurányi, M. Gysel, B. Neininger, B. Schneider, C. Hueglin, A. Ulrich, A. Wichser, S. Henne, D. Brunner, R. Kaegi, M. Schwikowski, L. Tobler, F. G. Wienhold, I. Engel, B. Buchmann, T. Peter, and U. Baltensperger (2011), Ground-based and airborne in-situ measurements of the Eyjafjallajökull volcanic aerosol plume in Switzerland in spring 2010, *Atmos. Chem. Phys. Disc., 11,* 12949-13002.

Carn, S. A., K.D. Froyd, B. E. Anderson, P. Wennberg, J. Crounse, K. Spencer, J.E. Dibb, N. A. Krotkov, E. V. Browell, J. W. Hair, G. Diskin, G. Sachse, and S. A. Vay (2011), In situ measurements of tropospheric volcanic plumes in Ecuador and Colombia during TC4, *J. Geophys. Res.*, doi:10.1029/2010JD014718, in press.

Casadevall, T. J. (1994). The 1989-1990 eruption of Redoubt volcano Alaska: impacts on aircraft operations. *Journal of volcanology and geothermal research*, *62*, 301-316.

Chazette, P. M. Bocquet, P. Royer, V. Winiarek, J.-C. Raut, P. Labazuy, M. Gouhier, M. Lardier, and J.-P. Cariou (this issue), Eyjafjallajökull ash concentrations derived from both lidar and modelling, *Submitted to J. Geophys. Res.*

Clarisse, L. F. Prata, J.-L. Lacour, D. Hurtmans, C. Clerbaux, and P.-F. A. Coheur (2010) A correlation method for volcanic ash detection using hyperspectral infrared measurements. *Geophys. Res. Lett., 37*, L19806.

Cotton, R., S. Osborne, Z. Ulanowski, E. Hirst, P. H. Kaye, and R. S. Greenaway (2009), The Ability of the Small Ice Detector (SID-2) to Characterise Cloud Particle and Aerosol Morphologies obtained during Flights of the FAAM BAe-146 Research Aircraft. *J. Atmos. Ocean. Tech., 27*, 290-303.

Chou, C., P. Formenti, M. Maille, P. Ausset, G. Helas, M. Harrison, and S. Osborne (2008), Size distribution, shape, and composition of mineral dust aerosols collected during the African Monsoon Multidisciplinary Analysis Special Observation Period 0: Dust and Biomass-Burning Experiment field campaign in Niger, January 2006, J. Geophys. Res., 113, D00C10, doi:10.1029/2008JD009897.

Dacre H. F., A. L. M. Grant, R. J. Hogan, S. E. Belcher, D. J. Thomson, B. Devenish, F. Marenco, J. M. Haywood, A. Ansmann, and I. Mattis (this issue), The structure and magnitude of the ash plume during the initial phase of the Eyjafjallajökull eruption, evaluated using lidar observations and NAME simulations, *Submitted to J. Geophys. Res.*

Devenish, B., (this issue), Case study modelling volcanic ash, *Submitted to J. Geophys. Res.*

Devenish, B., D.J. Thomson, F. Marenco, S.J. Leadbetter, H. Ricketts (2011), A study of the arrival over the United Kingdom in April 2010 of the Eyjafjallajökull ash cloud using ground-based lidar and numerical simulations, *Submitted to Atmos. Environ.*

Dubovik O, Sinyuk A, Lapyonok T, Holben BN, Mishchenko M, Yang P, Eck TF, Volten H, Mu˜noz O, Veihelmann B, van der Zande WJ, Leon J-F, Sorokin M, Slutsker I. 2006. Application of spheroid models to account for aerosol particle nonsphericity in remote sensing of desert dust. *J. Geophys. Res.* **111**: D11208, DOI:10.1029/2005JD006619.

EUFAR, European facility for airborne research, available at: http://www.eufar.net/wiki/pmwiki/pmwiki.php/EufarCMS/VolcanicAshes?skin=view

EU (European Union), available at: http://ec.europa.eu/transport/doc/2010 06 30 volcano crisis report.pdf

Flentje, H., H. Claude, T. Elste, S. Gilge, U. Kohler, C. Plass-Dulmer, W. Steinbretch, W. Thomas, A. Werner, and W. Fricke (2010), The Eyjafjallajokull eruption in April 2010- detection of volcanic plume using in-situ measurements, ozone sondes and lidar-ceilometer profiles, *Atmos. Chem. Phys., 10*, 20, 10085-10092.

Formenti, P., J. L. Rajot, K. Desboeufs, S. Caquineau, S. Chevaillier, S. Nava, A. Gaudichet, E. Journet, S. Triquet, S. Alfaro, M. Chiari, J.M. Haywood, H. Coe, and E. Highwood (2008), Regional variability of the composition of mineral dust from western Africa: Results from the AMMA SOP0/DABEX and DODO field campaigns, *J. Geophys. Res., 113*, D00C13, doi:10.1029/2008JD009903.

Francis P.N., and M. C. Cooke (this issue), Retrievals of volcanic ash physical properties using SEVIRI radiances: Application to the Eyjafjallajökull eruption in April and May 2010, *Submitted to J. Geophys. Res.*

Gasteiger, J., S. Groß, V. Freudenthaler, and M. Wiegner (2011), Volcanic ash from Iceland over Munich: mass concentration retrieved from ground-based remote sensing measurements, *Atmos. Chem. Phys., 11*, 2209-2223, doi:10.5194/acp-11-2209-2011.

Gerbig, C., S. Schmitgen, D. Kley, A. Volz-Thomas, K. Dewey, and D. Haaks (1999), An improved fast-response vacuum-UV resonance fluorescence CO instrument, *J. Geophys. Res.*, *104* (D1), 1699-1704.

Gislason, S. R., T. Hassenkam, S. Nedel, N. Bovet, E. S. Eiriksdottir, H. A. Alfredsson, C. P. Hem, Z. I. Balogh, K. Dideriksen, N. Oskarsson, B. Sigfusson, G. Larsen, and S. L. S. Stipp (2011), Characterization of Eyjafjallajökull volcanic ash particles and a protocol for rapid risk assessment, PNAS, *108,* 7307-7312.

Grant, A. L. M., Dacre, H. and et al. (this issue), Horizontal and vertical structure of the Eyjafjallajökull ash cloud over the UK, a comparison of airborne lidar observations and simulations, *submitted to J. Geophys. Res.*

Gudmundsson, M. T., T. Thordarson, A. Ho¨skuldsson, G. Larsen, I. Jonsdottir, B. Oddsson, E. Magnusson, T. Hognadottir, G. Sverrisdottir, N. Oskarsson, T. Thorsteinsson, K. Vogfjord, H. Bjornsson, G. N. Pedersen, S. Jakobsdottir, S. Hjaltadottir, M. Roberts, G. B. Gudmundsson, S. Zophoniasson, and F. Hoskuldsson (2010), The Eyjafjallajokull eruption in April–May 2010; course of events ash generation and ash dispersal, *AGU Annual Meeting* 2010, San Francisco, USA.

Guffanti, M., T. J. Casadevall, K. Budding (2010a). Encounters of aircraft with volcanic ash clouds; A compilation of known incidents, 1953-2009: U.S. Geological Survey Data Series 545, ver. 1.0, 12 p., plus 4 appendixes including the compilation database, available at http://pubs.usgs.gov/ds/545

Guffanti, M., D. J. Schneider, K. L. Wallace, T. Hall, D. R. Bensimon, and L. J. Salinas (2010b), Aviation response to a widely dispersed volcanic ash and gas cloud from the August 2008 eruption of Kasatochi, Alaska, USA, *J. Geophys. Res., 115*, D00L19, doi:10.1029/2010JD013868.

Hand V.L. Capes G.,Vaughan D.J.,Formenti P., Haywood J.M. and Coe H, Evidence of internal mixing of African dust and biomassburning particles by individual particle analysis using electron beam techniques., J. Geophys. Res, 115, D13301, doi:10.1029/2009JD012938, 2010

Harrison R.G., K. A. Nicoll, Z. Ulanowski, and T. A. Mather (2010), Self-charging of the Eyjafjallajökull volcanic ash cloud, *Environ. Res. Lett. 5*, 024004, doi:10.1088/1748-9326/5/2/024004.

Haywood, J., P. Francis, O. Dubovik, M. Glew, and B. Holben (2003), Comparison of aerosol size distributions, radiative properties, and optical depths determined by aircraft observations and Sun photometers during SAFARI 2000, *J. Geophys. Res., 108*(D13), 8471, doi:10.1029/2002JD002250.

Hess, M. P., P. Koepke, and I. Schultz (1998), Optical properties of aerosol and clouds: The software package OPAC. *Bulletin of the American Meteorological Society, 79*, 831-844.

Hesse, E. (2008), Modelling diffraction during ray-tracing using the concept of energy flow lines. *J. Quant. Spectrosc. Radiat. Transfer, 109*, 1374-1383.

Hirst, E., P. H. Kaye, R. S. Greenaway, P. Field, D. W. Johnson (2001), Discrimination of micrometre-sized ice and super-cooled droplets in mixed-phase cloud. *Atmos. Environ, 35*, 33-47.

Hobbs, P. V., J. P. Tuell, D. A. Hegg, L. F. Radke, and M. W. Eltgrowth (1982), Particles and gases in the emissions from the 1980–1981 volcanic eruptions of Mt. St. Helens, *J. Ge ophys. Res., 87,* 11,062–11,086, doi:10.1029/JC087iC13p11062.

Hobbs, V. P., Radke, L. F., Lyons, J. H., Ferek, R. J., Coffman, D. J., and Casadevall, T. J. (1991), Airborne measurements of particle and gas emissions from the 1990 volcanic eruptions of Mount Redoubt, J. Geophys. Res., 96, 18735–18752, 1991.

Hogan,R. J., J. M. Haywood, C. D. Westbrook, H. F. Dacre, F. Marenco, E. J. O'Connor, C. L. Wrench, and S. E. Belcher (this issue), Combined lidar and sunphotometer retrievals of ash particle size and mass concentration from the Eyjafjallajökull volcano, *Submitted to J. Geophys. Res.*

Holben B.N., T.F.Eck, I.Slutsker, D.Tanre, J.P.Buis, A.Setzer, E.Vermote, J.A.Reagan, Y.Kaufman, T.Nakajima, F.Lavenu, I.Jankowiak, and A.Smirnov (1998), AERONET - A federated instrument network and data archive for aerosol characterization, *Rem. Sens. Environ., 66*, 1-16.

Horwell C. J. (2007), Grainsize analysis of volcanic ash for the rapid assessment of respiratory health hazard *J. Env. Monitoring, 9* 1107–1115.

Hunton, D. E., A. A. Viggiano, T. M. Miller, J. O. Ballenthin, J. M. Reeves, J. C. Wilson, S.-H Lee, B. E. Anderson, W. H. Brune, H. Harder, J. B. Simpas, and N. Oskarsson (2005), In-situ aircraft observations of the 2000 Mt. Hekla volcanic cloud: Composition and chemical evolution in the Arctic lower stratosphere, *J. Volcan. Geothermal Res., 145*, 23–34.

James, M. R., J. S. Gilbert, and S. J. Lane (2002), Experimental investigation of volcanic particle aggregation in the absence of a liquid phase, *J. Geophys. Res., 107*(B9), 2191, doi:10.1029/2001JB000950.

James, M. R., S. J. Lane, and J. S. Gilbert (2003), Density, construction, and drag coefficient of electrostatic volcanic ash aggregates, *J. Geophys. Res., 108*(B9), 2435, doi:10.1029/2002JB002011.

Johnson, B.T. and S.R. Osborne (2011), Physical and optical properties of mineral dust aerosol measured by aircraft during the GERBILS campaign, *Q.J.R.M.S., 137*, in press.

Kokhanovsky, A. A. (2003), Optical properties of irregularly shaped particles. *J. Phys. D. 36*, 915–923.

Korolev, A. V., J. W. Strapp, G. A. Isaac, A. N. Nevzorov (1998a), The Nevzorov Airborne Hot-Wire LWC–TWC Probe: Principle of Operation and Performance Characteristics. *J. Atmos. Oceanic Technol.*, **15**, 1495–1510.

Korolev, A. V., J. W. Strapp, G. A. Isaac, (1998b) Evaluation of the Accuracy of PMS Optical Array Probes. *J. Atmos. Oceanic Technol.*, **15**, 708–720.

Leadbetter, S., and M. Hort (2011), Volcanic ash hazard climatology for an eruption of Hekla Volcano, Iceland, *Journal of Volcanology and Geothermal Research, 199*, 230-241.

Lee et al. (this issue), Observations of volcanic ash from lidar and cloud-base recorders, *submitted to J. Geophys. Res.*

Luke, W. T: Evaluation of a commercial pulsed fluorescent detector for the measurements of low-level SO2 concentrations during the Gas-Phase Sulfur Intercomparison Experiment, *J. Geophys. Res., 102 (D13)*, 16255-16265, 1997.

Macke, A., J. Mueller, E. Raschke (1996), Single scattering properties of atmospheric ice crystals, *J. Atmos. Sci., 53*, 2813–2825.

Marenco, F., B. Johnson, K. Turnbull, S. Newman, J. Haywood, H. Webster, and H. Ricketts (2011), Airborne lidar observations of the 2010 Eyjafjallajökull volcanic ash plume, J. Geophys. Res., 116, D00U05, doi:10.1029/2011JD016396.

Marenco, F., and R. J. Hogan (2011), Determining the contribution of volcanic ash and boundary layer aerosol in backscatter lidar returns:
A three-component atmosphere approach, J. Geophys. Res., 116, D00U06, doi:10.1029/2010JD015415.

Mastin et al. (2009), A multidisciplinary effort to assign realistic source parameters to models of volcanic ash-cloud transport and dispersion during eruptions, *J. Volcan. Geotherm. Res.,186* (1-2), 10-21.

Millington, S.C. (this issue), Simulated volcanic ash imagery: a method to compare NAME ash concentration forecasts with SEVIRI imagery for the Eyjafjallajökull eruption in 2010. *Submitted to J. Geophys. Res.*

Navratil T., J. Hladil, L. Strnad, L. Koptikova1, and R. Skala (this issue), Evidence of volcanic ash particulate matter from the 2010 Eyjafjallajökull eruption in dust deposition at Prague-Suchdol Central Europe, *submitted to J. Geophys. Res.*

Newman, S., L. Clarisse, F. Marenco, S. Havemann, B. Johnson, K. Turnbull, J. Haywood (this issue), A case study of observations of volcanic ash from the Eyjafjallajökull eruption. Part 2: airborne and satellite radiative measurements, *submitted to J. Geophys. Res.*

Osborne SR, Baran AJ, Johnson BT, Haywood JM, Hesse E, Newman S. 2011. Short-wave and long-wave radiative properties of Saharan dust aerosol. Q. J. R. Meteorol. Soc. DOI:10.1002/qj.771

Osborne, S.R., B.T. Johnson, J.M. Haywood, A.J. Baran, M.A.J. Harrison and C.L. McConnell, Physical and optical properties of mineral dust aerosol during the Dust and Biomass-burning Experiment, *J. Geophys. Res., 113*, D00C03, 2008.

Oskarsson N. (2010), Chemical analysis of rocks from the Eyjafjallajökull 2010 eruptions, *Reported at http://www.earthice.hi.is/page/IESEYCEMCOM*

Patterson, E., M. (1981), Measurements of the Imaginary Part of the Refractive Index between 300 and 700 Nanometers for Mount St. Helens Ash, *Science, 211*, 836 -838.

Patterson, E. M., C. O. Pollard (1983), Optical properties of the ash from El Chichon volcano, *Geophys. Res. Lett., 10* (4), 317-320.

Pollack, J. B., O. B. Toon, and B. N. Khare (1973) Optical properties of some terrestrial rocks and glasses *Icarus, 19,* 372–389.

Prata, A. J., and A. Tupper (2009) Aviation hazards from volcanoes: the state of the science, *Nat.Hazards, 51*, 239–244, 5543

Pyle, D.M., M. L. I. Witt, C. J. Horwell, J. S. Le Blond (this issue), Distal fallout of Eyjafjallajökull ash over Europe: implications for respiratory health hazard during future Icelandic eruptions. *Submitted to Journal of Geophysical Research Special Issue.*

Radke, L. F., P. V. Hobbs, and J. L. Stith (1976), Airborne measurements of gases and aerosols from volcanic vents on Mt. Baker, *Geophys. Res. Lett., 3*, 93–96, doi:10.1029/GL003i002p00093.

Renfrew, I. A., Petersen, G. N., Sproson, D. A. J., Moore, G. W. K., Adiwidjaja, H., Zhang, S. and North, R. (2009), A comparison of aircraft-based surface-layer observations over Denmark Strait and the Irminger Sea with meteorological analyses and QuikSCAT winds. Quarterly Journal of the Royal Meteorological Society, 135: 2046–2066. doi: 10.1002/qj.444

Rose, W. I., R. L. Chuan, R. D. Cadle, and D. C. Woods (1980), Small particles in volcanic eruption clouds, *Am. J. Sci., 280*, 671–696, doi:10.2475/ajs.280.8.671.

Rose, W.I., et al., (2006), Atmospheric chemistry of a 33-34 hour old volcanic cloud from Hekla volcano (Iceland): insights from direct sampling and the application of chemical box modeling, *J. Geophys. Res., 111*, D20206, doi:10.1029/2005JD006872.

Royer, P., P. Chazette, A. Dabas, M. Lardier, and L. Gomez (2011), Retrieval of mass concentration in the volcanic ash plume from Eyjafjallajökull eruption using airborne ground-based and in-situ measurements, poster presentation at EGU, April, 2011.

Schumann, U., B. Weinzerl, O. Reitebuch, H. Schlager, A. Minikin, C.Forster, R. Baumann, T. Sailer, K. Graf, H. Mannstein, C. Voigt, S. Rahm, R. Simmet, M. Scheibe, M. Lichtenstern, R. Stock, H. Rüba, D. Schäuble, A. Tafferner, M. Rautenhaus, T. Gerz, H. Ziereis, M. Krautstrunk, C. Mallaun, J.-F. Gayet, K. Lieke, K. Kandler, M. Ebert, S. Weinbruch, A. Stohl, J. Gasteiger, S. Gross, V. Freudenthakerm N, Wiegner, A. Ansmann, M. Tesche, H. Olafsson, and K. Sturm (2011), Airborne observations of the Eyjafjallajökull volcano ash cloud over Europe during air space closure in April and May 2010, *Atmos. Chem Phys., 11*, 2245-2279.

SEPA 2010. Scotticsh Environment Protection Agency report: (http://www.sepa.org.uk/about_us/news/2010/volcanic_ash_cloud_%E2%80%93_the_lat-3.aspx)

Shipley, S., Sarna-Wojcicki, A.M., 1982, Distribution, thickness, and mass of Late Pleistocene and Holocene tephra from major volcanoes in the northwestern United States: a preliminary assessment of hazards from volcanic ejecta to Nuclear reactors in the Pacific Northwest: U.S. Geological Survey Miscellaneous Field Studies Map MF-1435. (or see: http://volcanoes.usgs.gov/ash/properties.html#density)

Sparks, R.S. J., M. I. Bursik, S. N. Carey, J. S. Gilbert, L. S. Glaze, H. Siggurdsson and A. W. Woods (1997), Volcanic Plumes, John Wiley and Sons, New York, 574pp.

Stohl A., A. J. Prata, S. Eckhardt, L. Clarisse, A. Durant, S. Henne, N. I. Kristiansen, A. Minikin, U. Schumann, P. Seibert, K. Stebel, H. E. Thomas, T. Thorsteinsson, K. Tørseth, and B. Weinzier (2011), Determination of time- and height-resolved volcanic ash emissions for quantitative ash dispersion modeling: the 2010 Eyjafjallajökull eruption, *Atmos. Chem. Phys. Disc., 11*, 5541-5588.

Tanré, D., J. M. Haywood, J. Pelon, J. F. Léon, B. Chatenet, P. Formenti, P. Francis, P. Goloub, E. J. Highwood, G. Myhre (2003), Measurement and modelling of the Saharan dust

radiative impact: Overview of the SaHAran Dust Experiment (SHADE), *J. Geophys. Res., 108*(D13): 8574, doi:10.1029/2002JD003273.

Thomas, H. E., and Prata, A. J (2011), Sulphur dioxide as a volcanic ash proxy during the April–May 2010 eruption of Eyjafjallajökull Volcano, Iceland, *Atmos. Chem. Phys. Discuss., 11,* 7757-7780, doi:10.5194/acpd-11-7757-2011.

Turnbull, K., B. Johnson, F. Marenco, J. Haywood, A. Woolley, et al. (this issue), A Case Study of Observations of Volcanic Ash from the Eyjafjallajökull eruption; in situ airborne observations. *Submitted to J. Geophys. Res.*

Ulanowski Z., E. Hesse, P.H. Kaye and A.J. Baran (2006), Light scattering by complex ice-analogue crystals, *J. Quantit. Spectr. Rad. Transf.*, 100, 382-392.

Ulanowski, Z., P.H. Kaye, E. Hirst & R.S. Greenaway (2010), Light scattering by ice particles in the Earth's atmosphere and related laboratory measurements, in Proc. 12th Int. Conf. Electromagnetic & Light Scatt., edited by K. Muinonen et al., pp. 294-297, University of Helsinki, Finland.

Ulanowski Z. and M. Schnaiter (2011), UV and visible light scattering and absorption measurements on aerosols in the laboratory, in Fundamentals and Applications of Aerosol Spectroscopy, edited by J. P. Reid and R. Signorell, pp. 243-268, CRC Press, Boca Raton.

Webster, H. N., I. P. C. Heard, B. J. Johnson, D. J. Thomson, K. Turnbull, F. Marenco, N. I. Kristiansen, J. Dorsey, A. Minikin, B. Weinzien, B. J. Devenish, M. C. Hort, and J. M. Haywood (this issue), A comparison of modelled and observed ash concentrations from the 2010 Eyjafjallajökull eruption, *Submitted to J. Geophys. Res.*

Witham, C. S., M. C. Hort, R. Potts, R. Servranckx, P. Husson, and F. Bonnardot (2007), Comparison of VAAC atmospheric dispersion models using the 1 November 2004 Grimsvötn eruption, *Meteorological Applications, 14,* 27-38.

Tables

Date	Flight number	Take off location / time (UTC)	Land location / time (UTC)	Comments on in-situ data collected
20 April	B521	Cranfield 1124	Cranfield 1702	Limited in-situ sampling due to flight plan restrictions. CAS not fitted.
21 April	B522 B523	Cranfield 1020 Prestwick 1340	Prestwick 1139 Prestwick 1856	Limited in-situ sampling due to flight plan restrictions.
22 April	B524 B525	Prestwick 1009 Prestwick 1635	Prestwick 1528 Cranfield 1722	Limited in-situ sampling due to low ambient concentrations
4 May	B526	Cranfield 1004	Cranfield 1551	Moderate concentrations of ash sampled over Irish Sea at 2-5km
5 May	B527	Cranfield 0911	Cranfield 1507	Moderate concentrations of ash sampled over Irish Sea & central England at 3-4km
14 May	B528 B528b	Cranfield 1007 Prestwick 1728	Prestwick 1542 Cambridge 1917	Substantial in-situ sampling of high concentrations over N. England - NW approaches of Scotland, 5-8km
16 May	B529	Cambridge 1225	Nantes 1810	Limited in-situ sampling from tops of ash layers (8km) over N. England and Scotland.
17 May	B530	Nantes 1126	Cambridge 1658	Substantial in-situ sampling, moderate concentrations ash over N. Sea at 3-7km, co-ordination with DLR Falcon (see Turnbull et al., 2011; Newman et al., 2011)
18 May	B531	Cambridge 0944	Cranfield 1454	Good in-situ sampling, moderate concentrations of ash over N. Sea at 2-4km

Table 1. Summary of all flights made by the FAAM aircraft during the volcanic ash episodes of April – May 2010.

Instrument & *processing method*	Size bins	Size range (volume-equivalent diameter, µm)	Assumed composition	Mass density (g/cm^3)	Refractive index	Particle shape
PCASP *Default*	2 – 16	0.13 – 0.62	Sulphuric acid	1.8	1.43 + 0i	Sphere
CAS *Default*	2 – 26	0.57 – 35.0	Mineral dust / ash	2.3	1.52 + 0.0015i	Irregular
CAS *Spherical moderately absorbing*	2 – 26	0.65 – 69.4	Mineral dust / ash	2.3	1.52 + 0.0015i	Sphere
CAS *Spherical highly absorbing*	2 – 26	0.66 – 80.0	Mineral dust / ash	2.3	1.59 + 0.004i	Sphere

Table 2: Data interpretation methodology / assumptions for the PCASP and CAS instrument. Size ranges in column 3 are results following calibration and refractive index corrections.

Flight number & Date	Number of ash cloud penetrations	Peak ash mass concentrations ($\mu g/m^3$)	Column mass loadings (g/m^2)
B522 & B523 (21 April)	2	50 – 60	0.01 – 0.05
B524 & B525 (22 April)	4	20 – 30	0.01 – 0.04
B526 (4 May)	5	30 – 160	0.01 – 0.06
B527 (5 May)	5	160 – 580	0.07 – 0.17
B528 (14 May)	21	650 – 4670	0.65 – 5.47
B528b (14 May)	4	130 – 490	0.02 – 0.11
B529 (16 May)	4	20 – 130	0 - 0.01
B530 (17 May)	7	220 – 500	0.23 – 0.73
B531 (18 May)	9	30 - 210	0.01 – 0.15

Table 3. Summary of ash penetrations including peak ash concentrations and column loadings from profiles (range of values is the range from top 3 profile maxima on each flight, ignoring profiles less than 50km apart).

Fit	D_g	σ
Lower	3.2	1.8
Middle (overall mean)	3.8	1.85
Upper	4.5	1.9

Table 4. Log-normal parameters for the fitted aerosol volume curves in Figure 3: volume geometric mean diameter (D_g) and standard deviation (σ).

Flight number & Date	k_{ext} total 550nm	k_{ext} coarse 355nm	k_{ext} coarse 550nm	k_{ext} coarse 680nm
B528 (4 May)	1.21	0.92	**0.93**	0.96
B527 (5 May)	0.80	0.65	**0.64**	0.65
B528 & B528b (14 May)	0.63	0.62	**0.62**	0.61
B529 (16 May)	0.95	0.82	**0.82**	0.82
B530 (17 May)	0.78	0.72	**0.72**	0.72
B531 (18 May)	0.83	0.74	**0.73**	0.73

Table 5. Flight averaged k_{ext} values for 355, 550 and 680nm for the total aerosol population (0.1 - 35μm) and the coarse mode (0.6 - 35μm).

Data source	Particle assumption	Coarse mode k_{ext} (m^2/g) (adjusted to 550nm and ρ=2300 kg/m^3)	
		Range	Best estimate
CAS (Table 4 and Fig 14)	Irregular ash	0.45 – 1.06	0.60
Log-normal fits to CAS	Irregular ash	0.57 – 0.77	0.66
Log-normal fits to CAS	Sphere	0.41 – 0.59	0.49
Hogan et al., 2011 (Chilbolton AERONET & lidar retrieval)	Aerated sphere (15% air, 75% ash)	n/a	1.00
Ansmann et al., 2011 (OPAC desert dust)	Sphere	n/a	0.58
Gasteiger et al. , 2011 (Munich AERONET & lidar retrieval)	Spheroid	0.49 - 1.23	0.78

Table 6. Comparison of k_{ext} values derived from different methods and different studies of ash from the 2010 eruption of Eyjafjallajökull.

Figures
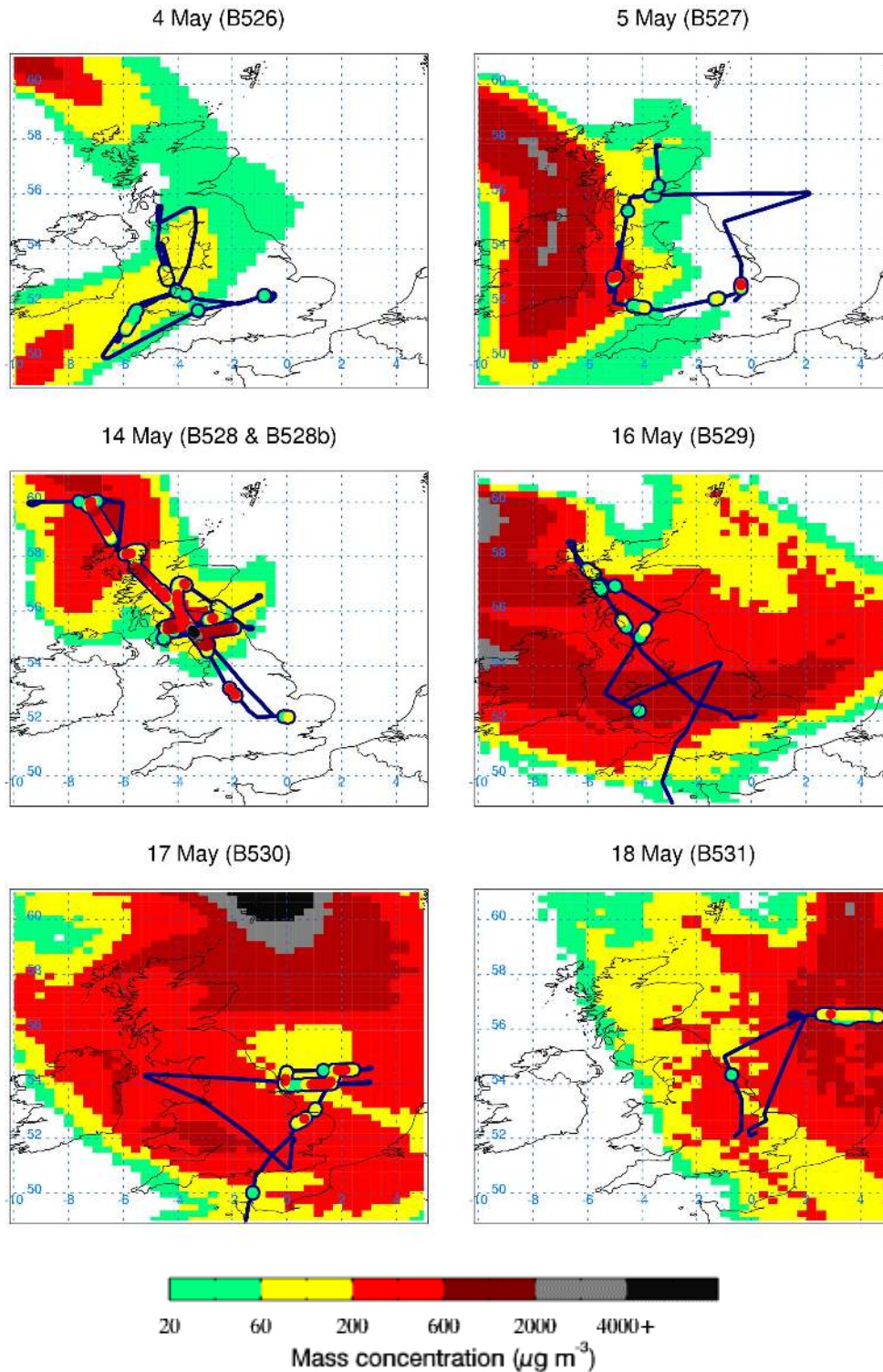
Figure 1. Flight tracks (dark blue) of the FAAM aircraft during ash flights 4 – 18 May with CAS ash concentration overlaid on the NAME forecast of peak ash concentration likely within the altitude range of FL000 – FL200 (roughly 0 – 6km) and between 12 – 18 UTC.
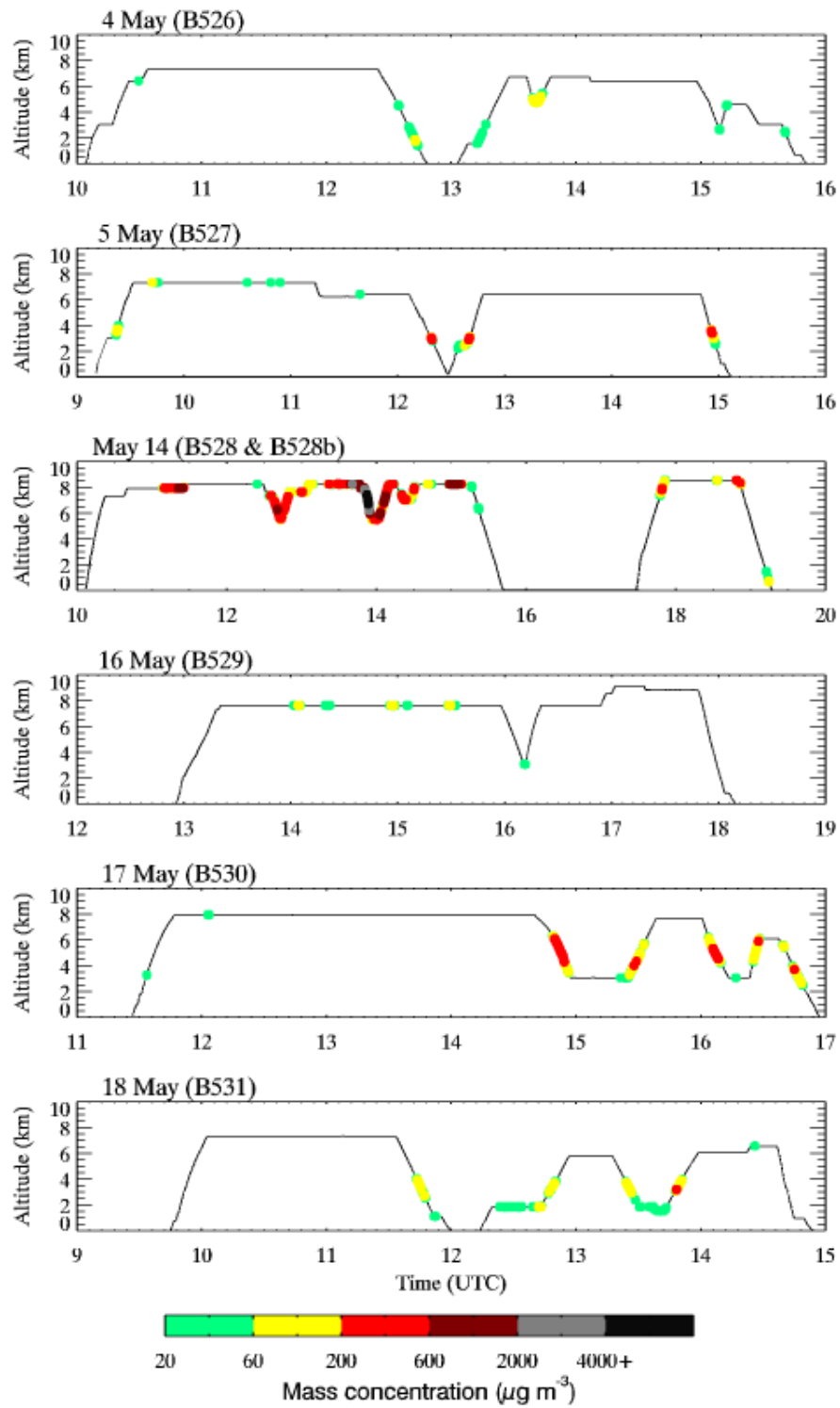
Figure 2. Estimated ash mass concentration from CAS as a function of the FAAM aircraft altitude and time during ash flights B526 – B531 (May 4 – May 18).
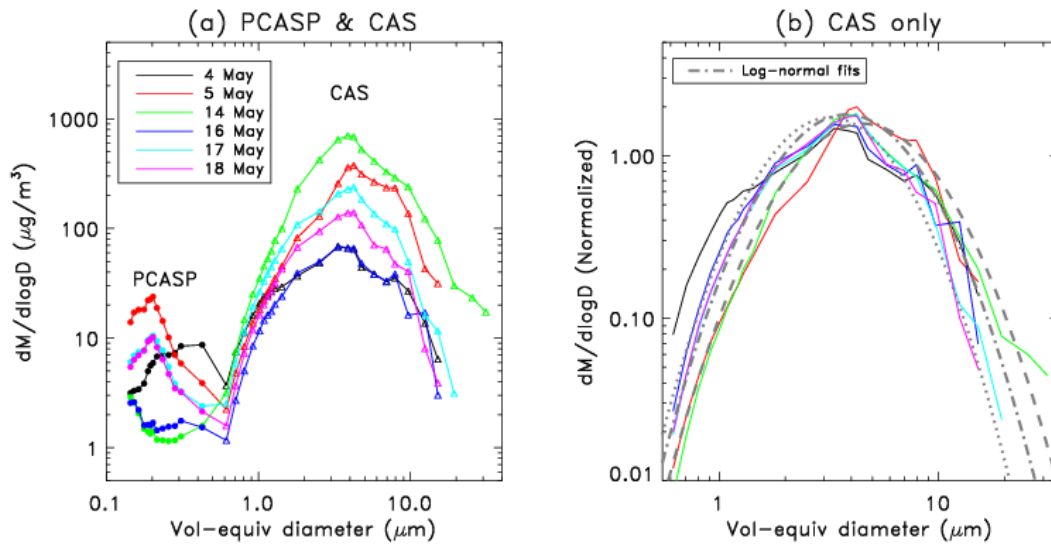
Figure 3. Aerosol size distributions by mass concentration (dM/dlogD) and volume-equivalent diameter (d_v) averaged over all ash cloud penetrations for each of the flights B526 – B531 (4 – 18 May). a) PCASP data plotted with circles, CAS data with triangles. b) CAS data only with normalized y-axis and the log-normal fits of Table 4: lower (dotted), middle (dot-dash), and upper (dashed line) fits.
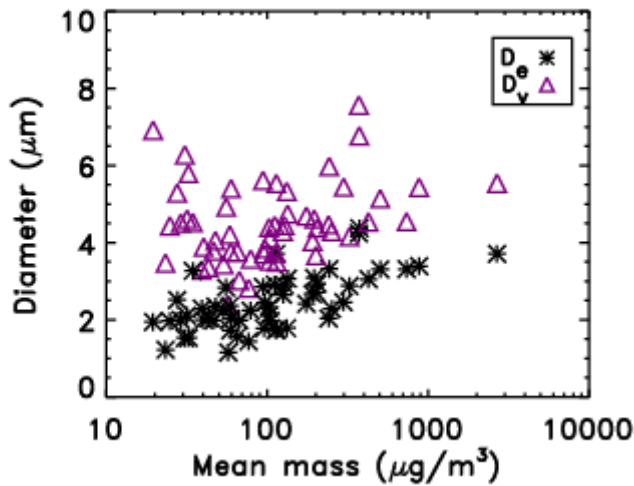
Figure 4. Variability of effective diameter (De) and volume-mean diameter (Dv) with mean ash mass concentration from all FAAM ash cloud penetrations.
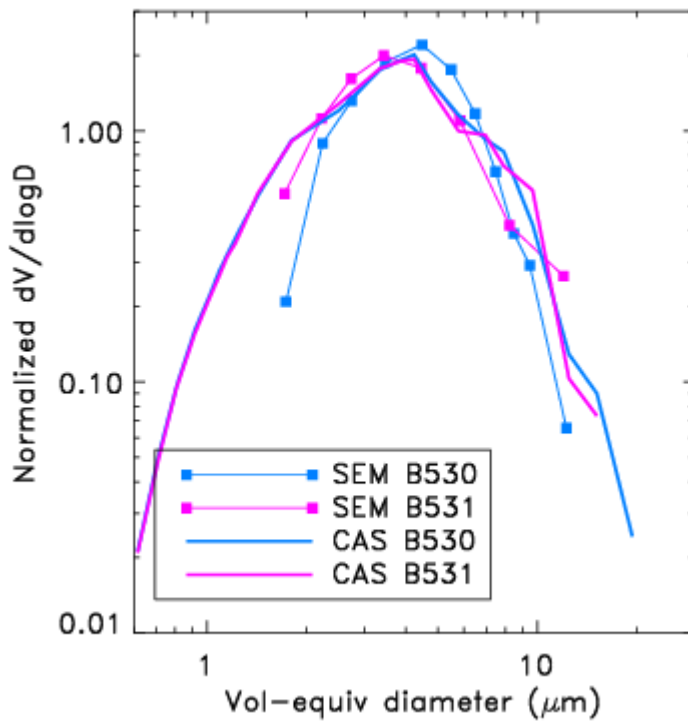
Figure 5. Normalized aerosol volume size distributions (dV/dlogD) from CAS (1 – 20µm only) and SEM analysis, averaged over flights B530 and B531 (17 & 18 May).
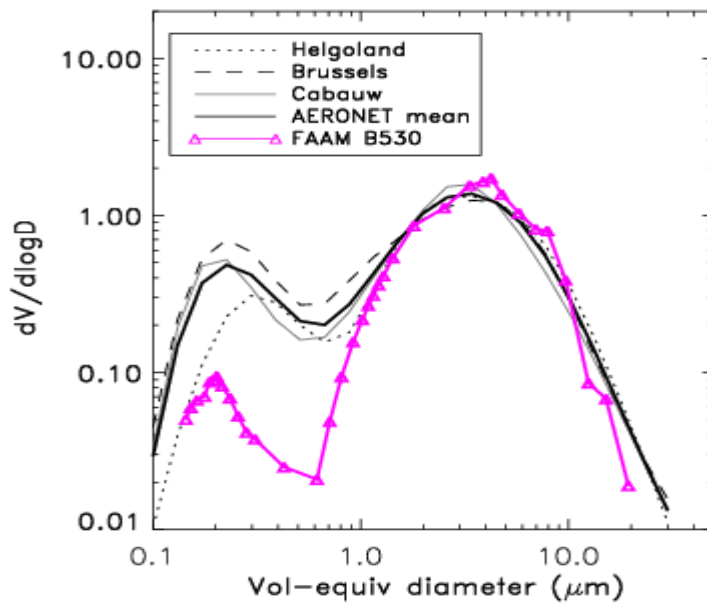
Figure 6. Normalized aerosol volume size distributions (dV/dlogD) from mean PCASP & CAS on flight B530 (17 May) and mean AERONET retrievals for 17 – 18 May from selected sites (see section 5.3.3), plus the mean from all three sites.
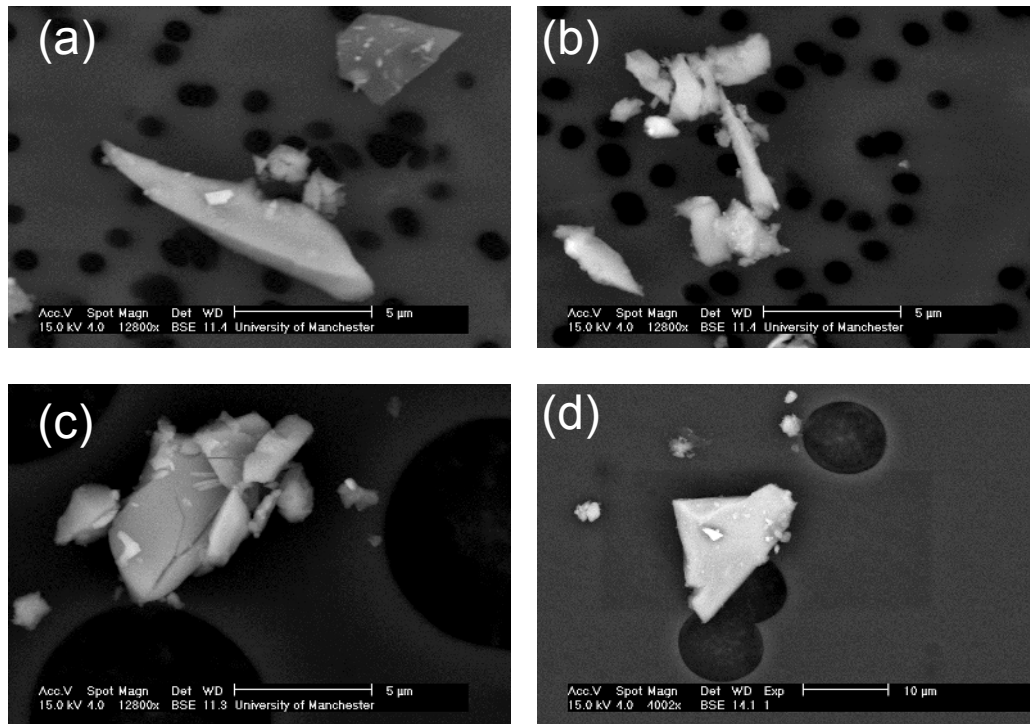
Figure 7. SEM images of ash particles collected on the FAAM aircraft filter system during flight B530 on 17 May (a – c) and B531 on 18 May (d): (a, b) from 1µm filter with 12800x magnification, (c) from 10µm filter with 12800x magnification, (d) from 10µm filter with 4002x magnification. Dark circles are the filter pores, the grey background is the Nucleopore filter substrate, and brighter shapes are the ash particles.
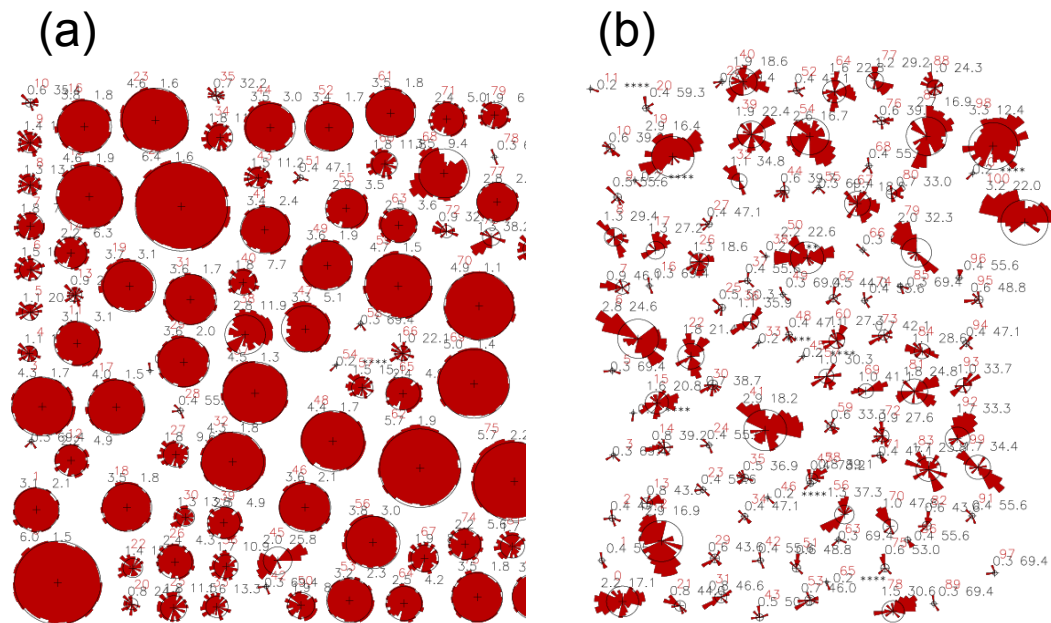
Figure 8. Azimuthal scattering patterns from the Small Ice Detector (SID-2H) probe on the FAAM aircraft for samples of aerosols found over the Irish sea at (a) 30m altitude and (b) 5km. The symmetric scattering patterns (a) indicate spherical aerosol (i.e. water droplets and/or hydrated sea salt) whereas the highly asymmetric patterns (b) indicate irregular non-spherical particles (i.e. ash). Pairs of black numbers above each pattern give particle radius (µm) and asphericity factor.
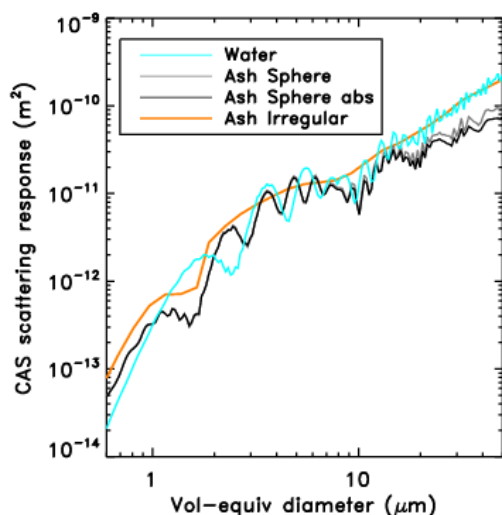
Figure 9. CAS scattering response (scattering cross-section, m^2) as a function of volume-equivalent diameter for water spheres (RI = 1.33 + 0i), ash spheres (RI = 1.52 + 0.0015i), more absorbing ash spheres (RI = 1.59 + 0.004i) and ash irregular-shaped particles (RI = 1.52 + 0.0015i).
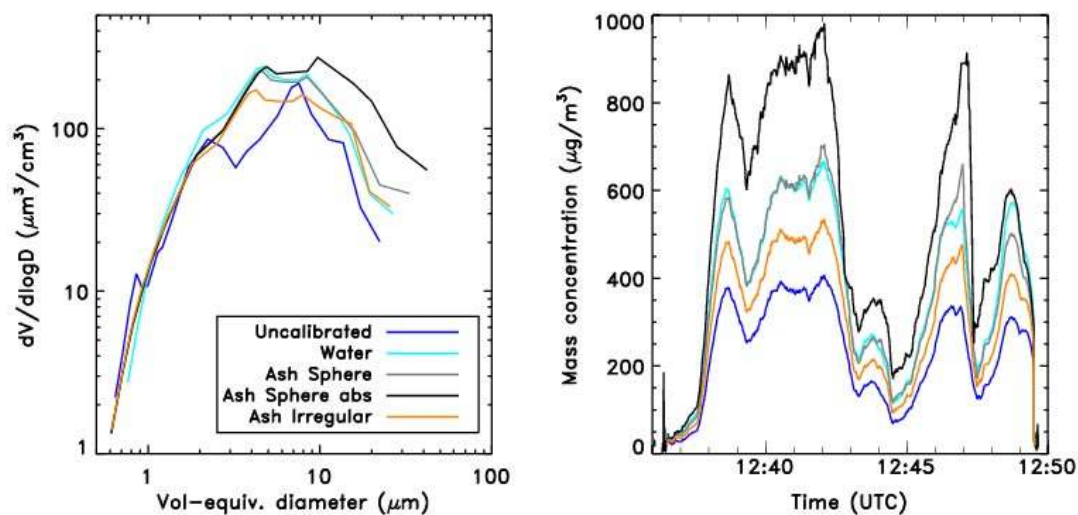

Figure 10. The influence of particle shape, refractive index and instrument calibration on the aerosol size distribution and estimation of ash mass concentration from CAS (based on a profile, 1236 – 1250UTC during flight B528, 14 May, ~60N, 7W).
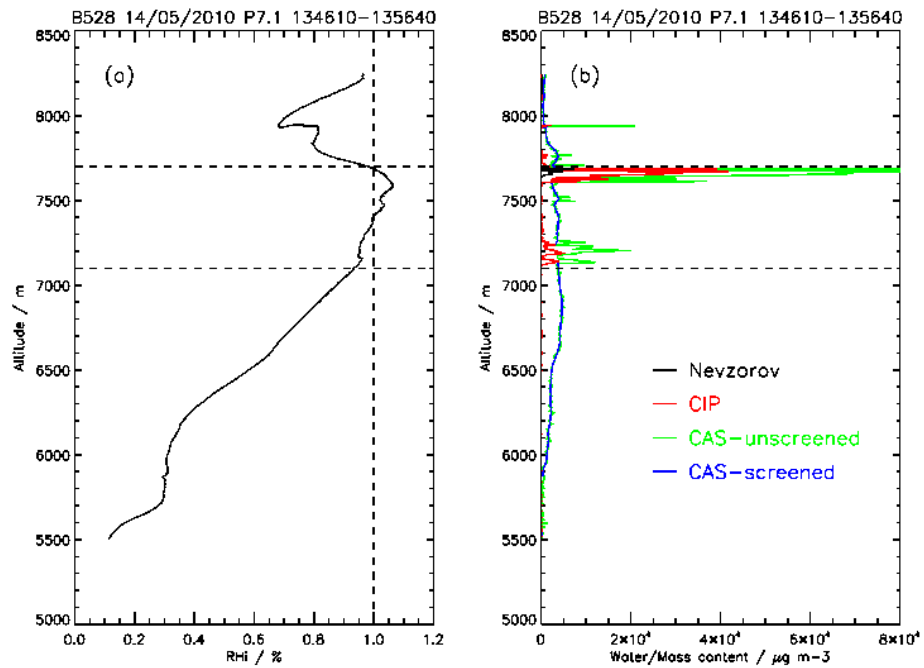
Figure 11. (a) Relative humidity with respect to ice during a profile descent of flight B528, 134610-135640UTC, 14 May 2010. The value is derived from frost-point temperature measurements using a GE1011B hygrometer. (b) Profiles of ice water content from the Nevzorov probe (black) and CIP-15 (red) together with the unscreened (green) and screened (blue) mass loadings from the CAS. The horizontal lines at 7100 and 7700m altitude arbitrarily mark the lower and upper bounds of the layer in which the CIP-15 detects ice particles.
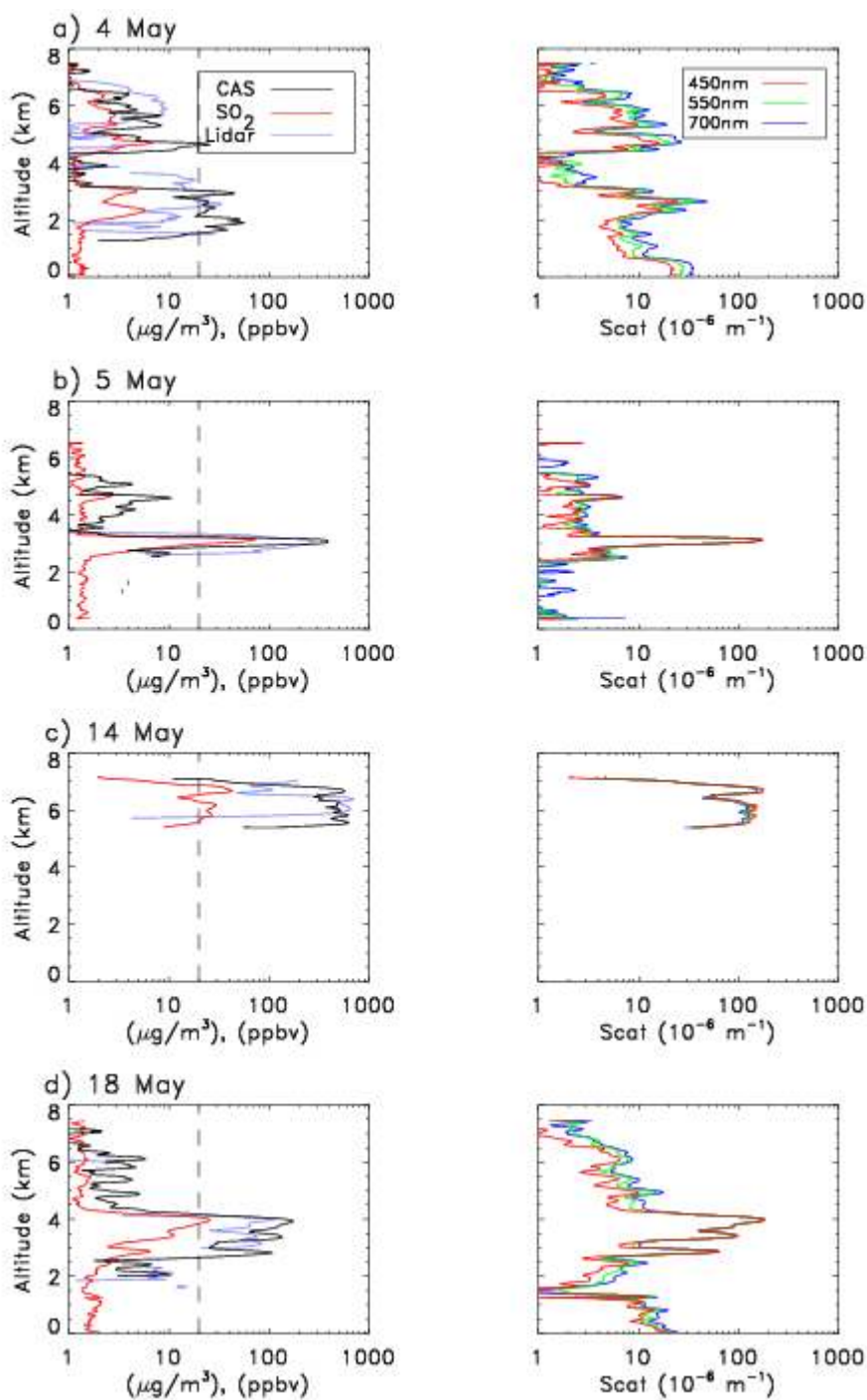
Figure 12. Vertical distributions of ash mass concentration derived from CAS and lidar (dashed line at the 20 μg/m³ threshold used to define ash plume penetrations in this study), SO₂ concentration, and nephelometer scattering coefficients for selected aircraft profiles: (a) 4 May (B526), 51.5°N 5.6°W, 1240UTC, 1660km downwind; (b) 5 May (B527), 53.0°N 5.1°W, 1220UTC, 1530km downwind; (c) 14 May (B528), 59.6°N 7.0°W, 1240UTC, 840km downwind; (d) 18 May (B531), 56.5°N 3.7°E, 1145UTC, 1260km downwind.
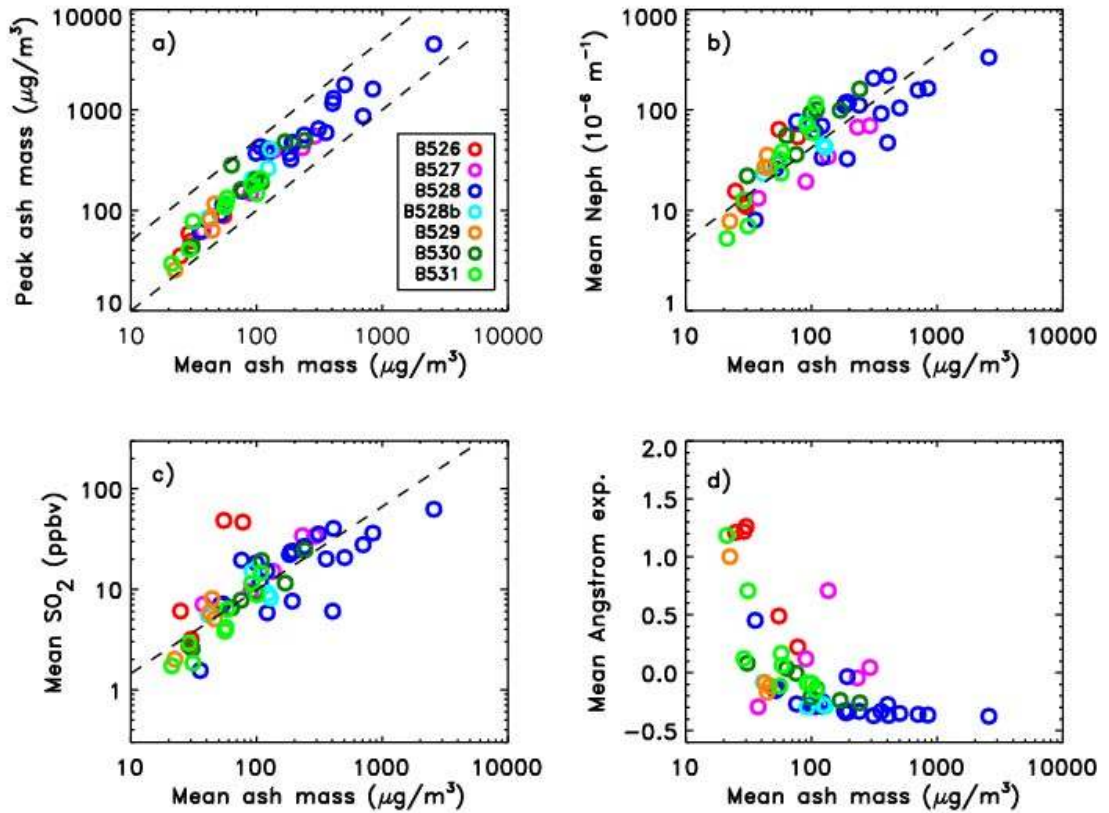
Figure 13: Correlations and variability of ash cloud properties including mean values of M_{ash} from CAS as compared to (a) peak M_{ash}, (b) mean nephelometer scattering coefficient at 550nm, (c) SO_2 concentration, and (d) Angstrom exponent. Dashed lines for (a) show the 1:1 and 5:1 line, other dashed lines are linear fits.
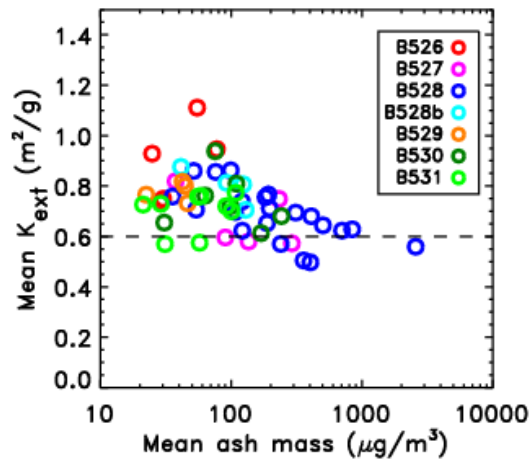

Figure 14. Coarse-mode specific extinction coefficient (k_{ext}) at 550nm estimated from the CAS size distribution as a function of mean ash mass during all FAAM ash cloud penetrations. Data processed using default particle property assumptions (Table 2).